Influenza-induced activation of recruited alveolar macrophages during the early inflammatory phase drives lung injury and lethality

Clarissa M Koch[1], Kishore R Anekalla[1], Yuan-Shih Hu[1], Jennifer M. Davis[1], Mark Ciesielski[1], Gaurav Gadhvi[2], Shang-Yang Chen[2], Margaret Turner[1], Yuan Cheng[1], Bria M Coates[1,3,4], Hiam Abdala-Valencia[1], Paul A Reyfman[1], Alexander V Misharin[1], GR Scott Budinger[1], Deborah R Winter[2±], Karen M Ridge[1,5±]

[1]Pulmonary and Critical Care Division, [2]Rheumatology Division, Department of Medicine, [3]Department of Pediatrics, Northwestern University Feinberg School of Medicine, Chicago, IL USA, [4]Ann & Robert H. Lurie Children's Hospital of Chicago, Chicago IL, [5]Department of Cell and Developmental Biology, Northwestern University Feinberg School of Medicine, Chicago, IL.

± Contributed equally to this paper

Corresponding author:

Karen M. Ridge, Ph.D.
Northwestern University
Feinberg School of Medicine
Division of Pulmonary and Critical Care Medicine
Simpson Querrey Biomedical Research Center
Department of Cell and Developmental Biology
303 E. Superior, 5-520
Chicago, IL 60611
Kridge@northwestern.edu
312-503-1648 – office

Abstract (155 words)

During infection with respiratory viruses, disease severity is linked to a hyperinflammatory endotype, characterized, in part, by increased levels of circulating cytokines and worse clinical outcomes. In this study, we identify gene expression patterns associated with three distinct phases (Infiltrating, Early Inflammatory, Late Inflammatory) in the influenza A virus response of recruited alveolar macrophages. In the Early Inflammatory phase, recruited macrophages begin expressing pro-inflammatory genes, driving cytokine-mediated lung damage and contributing to the morbidity observed in influenza-infected wild-type mice. In mice lacking vimentin (*Vim*$^{-/-}$), genes associated with the Early Inflammatory phase are suppressed, while the expression of the Infiltrating Phase genes is maintained, which is associated with protection from influenza-induced injury. Using a bone-marrow chimera mouse model, we validate that *Vim*$^{-/-}$ recruited alveolar macrophages are sufficient to confer protection from influenza-induced mortality. Our results define the temporal dynamics of gene expression in recruited alveolar macrophages, which shape the host response to infection with respiratory viruses.

Introduction

Recovery from viral pneumonia is a clinically important yet understudied process. A recent collaborative study from our group and others determined that viruses are the most common pathogens identified in patients with community-acquired pneumonia[1]. Severe viral pneumonia due to influenza A virus (IAV) or severe acute respiratory syndrome coronavirus 2 (SARS-CoV-2), the etiologic agent of coronavirus disease 2019 (COVID-19), damages the lower respiratory tract to cause acute respiratory distress syndrome (ARDS)[2]. Unremitting respiratory failure in patients with ARDS is a consequence of persistent inflammation and the failure of normal mechanisms of inflammation resolution and lung tissue repair. This hypothesis is clinically supported by a recent analysis of patients enrolled in the ARDSnet, in which patients with a hyperinflammatory endotype of ARDS, characterized in part by increased levels of circulating cytokines and chemokines, had worse clinical outcomes[3]. This points to the importance of a balanced and regulated immune response, where infection can be controlled while keeping tissue damage to a minimum.

Macrophages are the lung's primary cells that initiate and orchestrate the immune response after IAV infection[4]. Shortly after IAV or SARS-CoV-2 infection, tissue-resident alveolar macrophages (TRAMs) are depleted, and monocyte-derived alveolar macrophages (MoAMs) are recruited into the lung[2,5,6]. MoAM recruitment has been associated with excessive or dysregulated cytokine and immune cell responses in humans and mice[2,3,5,7]. Upon entering the infected lung, MoAMs express genes driving an inflammatory phenotype that contributes to persistent inflammation during the course of viral pneumonia resulting in

74 acute lung injury. Preventing the recruitment of these macrophages into the lung by
75 deleting CCR2 or its ligand reduces the severity of IAV infection without affecting viral
76 clearance[5]. Viral infections are sensed in host cells by pattern recognition receptors (PRR),
77 such as the NOD-like receptor family, pyrin domain containing 3 (NLRP3). A crucial step in
78 the immune response to IAV is the activation of the NLRP3 inflammasome and the
79 subsequent secretion of inflammatory cytokines, IL-1β, and IL-18[5,8-10]. Inhibition of the
80 NLRP3 inflammasome early in IAV infection impairs viral clearance and increases morbidity
81 and mortality in mice[11]. In contrast, inhibition of the NLRP3 inflammasome post-viral
82 clearance reduces inflammation-induced tissue damage and promotes lung repair[10,11]. As
83 a result, therapies that target these macrophages may be of interest[5,12,13]; however, no
84 study has yet investigated the time-dependent functions of MoAMs in response to influenza
85 A virus infection.
86
87 Vimentin, a type III intermediate filament, is ubiquitously expressed in macrophages and
88 plays a role in several critical immune response processes. Vimentin suppresses
89 inflammation in a mouse model of colitis[14] and alters inflammatory gene expression in
90 microglia lacking vimentin in a murine model of Alzheimer's disease[15]. Vimentin has been
91 described as a ligand for some PRRs, such as the nucleotide-binding oligomerization
92 domain-containing protein 2 (NOD2), and this interaction is required for subsequent NF-κB
93 activation[16]. We, and others, showed that vimentin is required for assembly and activation
94 of the NLRP3 inflammasome[17,18] and that vimentin-null (*Vim*$^{-/-}$) mice are protected from
95 LPS-induced lung injury by suppressing NLRP3 pro-inflammatory cytokines[17]. These

96 studies support the notion that vimentin may play a role in macrophage immune response
97 to IAV infection.
98
99 In this study, we use a mouse model of IAV to demonstrate that *vimentin-null (Vim$^{-/-}$)* mice
100 are protected from the lung damage and mortality associated with severe viral pneumonia.
101 Furthermore, we perform RNA-seq on MoAMs over a 6-day time-course following IAV
102 infection to characterize the immune response. We define temporal gene expression
103 patterns associated with three phases of IAV response in which MoAMs exhibit distinct
104 biological functions. Next, we compare these results to the same RNA-seq time course in
105 *Vim$^{-/-}$* MoAMs to determine which gene expression patterns and biological pathways
106 contribute to the observed protection. Finally, we generate *Vim$^{-/-}$* bone marrow chimeras to
107 test the role of MoAMs in response to IAV infection. Together, our results indicate that the
108 activation of MoAMs in the Early Inflammatory phase of IAV response drives lung damage
109 and lethality.
110
111 **Results**
112
113 **Vimentin null mice are protected from influenza-induced lung injury and mortality**
114 Our group have recently reported that persistent inflammation in patients with severe
115 SARS-CoV-2 pneumonia is sustained via stable circuits between alveolar macrophages
116 and T cells[2]. Using single-cell RNA-seq, four distinct clusters of monocytes-derived
117 alveolar macrophages (MoAMs) isolated from bronchoalveolar lavage fluid collected from
118 patients with severe SARS-CoV-2 pneumonia were identified (**Figure 1a, Supplemental**
119 **Figure 1a**)[2]. By querying this dataset, we found that *VIM* was among the genes differentially

120 expressed between MoAM1 and MoAM3: with highest expression in MoAM1 and
121 decreasing in MoAM3 (**Figure 1b,c)**. MoAM1 cluster was characterized by high expression
122 of pro-inflammatory cytokine genes, such as *IL1B, CXCL2, and CCL3* and low expression
123 of macrophage markers *MRC1* and *C1QA* (**Figure 1c,d)**. In contrast, cluster MoAM3
124 exhibited the highest expression of *MRC1, C1QA, and MERTK. MERTK* encodes a
125 receptor necessary for phagocytosis of apoptotic cells – a process which has been
126 mechanistically linked to a change in macrophage phenotype from pro-inflammatory to pro-
127 resolving[19,20] (**Figure 1c, d).** VIM expression did not vary between the two clusters
128 annotated as tissue-resident alveolar macrophages (TRAMs) (**Supplemental Figure**
129 **1b)**.This data from patients with severe SARS-CoV-2 pneumonia suggests that a higher
130 level of *VIM* expression in MoAMs is associated with a pro-inflammatory phenotype in viral
131 pneumonia, while MoAM with a pro-resolving phenotype was characterized by decreased
132 *VIM* expression.
133
134 Next, we used a clinically relevant murine model of viral pneumonia induced by the
135 influenza A virus to examine whether the loss of vimentin dampens the host immune
136 response. Wild-type (WT) and *Vim*$^{-/-}$ mice were infected with a lethal dose of IAV (Strain
137 A/WSN/1933 (H1N1), 200 pfu) and assessed for morbidity and mortality. WT mice had a
138 100% mortality rate, whereas <17% of the *Vim*$^{-/-}$ mice died by 10 days post-infection (p.i.)
139 (**Figure 1e**). By 14 days p.i., the 50% of surviving *Vim*$^{-/-}$ mice had recovered from mild
140 lethargy, coat ruffling, febrile shaking, and eye-watering. *Vim*$^{-/-}$ mice exhibited a lower wet-
141 to-dry lung weight ratio and decreased total protein concentration in bronchoalveolar lavage
142 fluid (BALF) than wild-type controls infected with IAV, indicating less damage to the

Figure 1

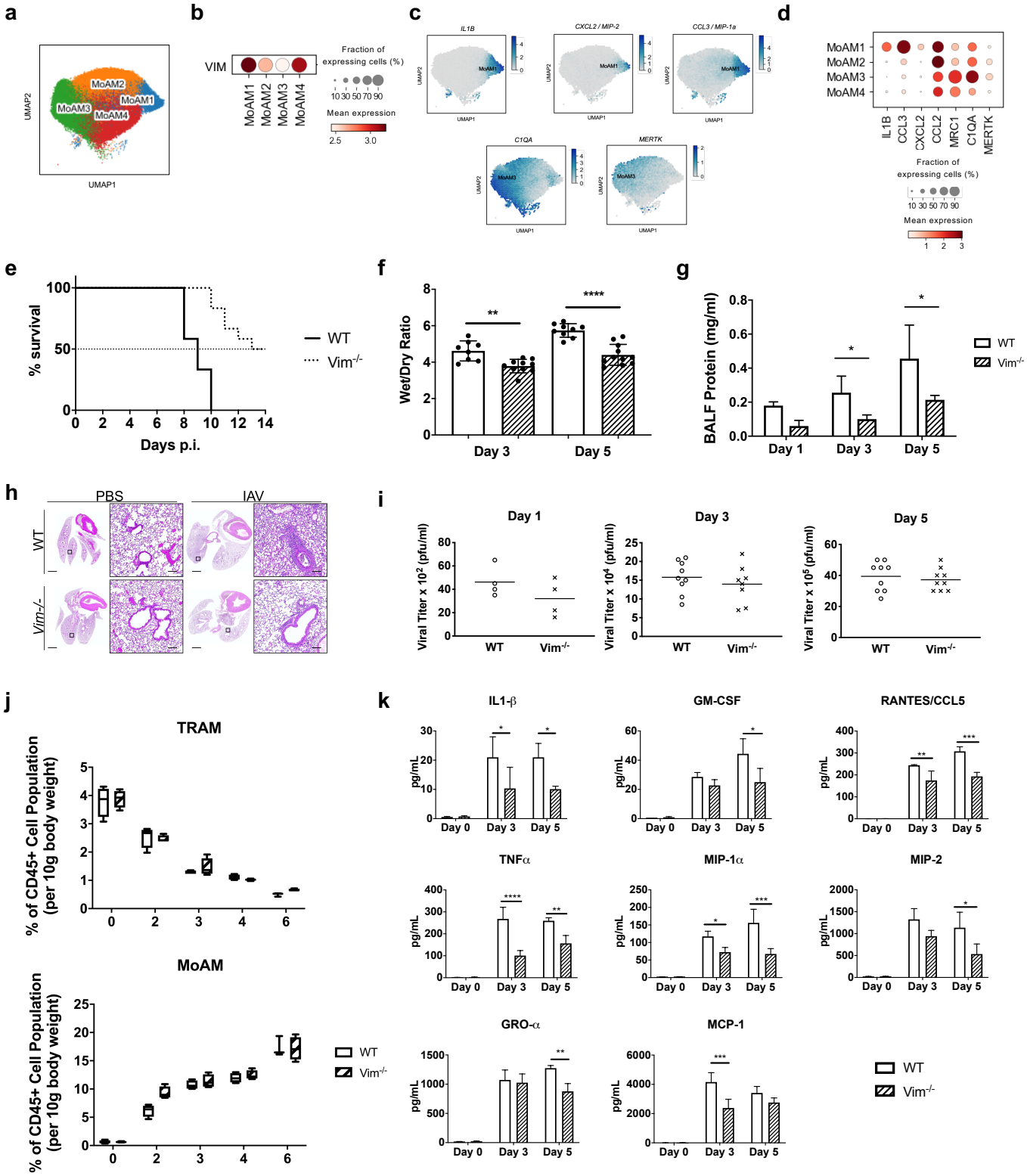
a
MoAM2
MoAM1
MoAM3
MoAM4
UMAP2
UMAP1
b
VIM
MoAM1
MoAM2
MoAM3
MoAM4
Fraction of expressing cells (%)
10 30 50 70 90
Mean expression
2.5 3.0
c
IL1B
CXCL2 / MIP-2
CCL3 / MIP-1a
C1QA
MERTK
d
MoAM1
MoAM2
MoAM3
MoAM4
IL1B
CCL3
CXCL2
CCL2
MRC1
C1QA
MERTK
Fraction of expressing cells (%)
10 30 50 70 90
Mean expression
1 2 3
e
% survival
Days p.i.
WT
Vim-/-
f
Wet/Dry Ratio
Day 3
Day 5
g
BALF Protein (mg/ml)
Day 1
Day 3
Day 5
WT
Vim-/-
h
PBS
IAV
WT
Vim-/-
i
Day 1
Day 3
Day 5
Viral Titer x 10^2 (pfu/ml)
Viral Titer x 10^4 (pfu/ml)
Viral Titer x 10^5 (pfu/ml)
WT
Vim-/-
j
TRAM
MoAM
% of CD45+ Cell Population (per 10g body weight)
WT
Vim-/-
k
IL1-β
GM-CSF
RANTES/CCL5
TNFα
MIP-1α
MIP-2
GRO-α
MCP-1
pg/mL
Day 0
Day 3
Day 5
WT
Vim-/-

Figure 1. Vimentin-null mice are protected from influenza-induced lung injury and mortality. a) Uniform Manifold Approximation and Projection (UMAP) of 40,248 cells annotated as monocyte-derived alveolar macrophages (MoAMs) obtained from 10 patients with severe COVID-19 disease within 48 hours after intubation. **b)** Fraction of cells expressing *VIM* and mean expression in each MoAM cluster. **c)** Visualization of *IL1-B, CCL3, CXCL2, C1QA*, and *MERTK* expression in MoAM cells using density projection plots. Scale bar represents expression averaged within hexagonal areas on UMAP. **d)** Fraction of cells expressing the representative genes and their mean expression in each MoAM cluster . **e)** Survival of wild-type (WT) and *Vim*$^{-/-}$ mice intratracheally infected with a lethal dose of influenza A virus (IAV) (200pfu) was measured and compared. Survival curves were analyzed using log-rank test, p-value =0.001. Data shown are n=12 per group. **f**) Lung wet-to-dry ratio measured at day 3 and 5 p.i. (n = 8-11/timepoint) **g**) Bronchoalveolar lavage fluid (BALF) protein levels measured by Bradford assay, n=5/timepoint. In **f** and **g**, differences between genotypes on each day were assessed by t-test. p-values were 0.0015 and <0.0001, for 3 and 5 days p.i., respectively. **h)** Representative images of murine lung architecture assessed by H&E staining, scale bar 100 um. **i**) Viral titer assessed by plaque assay. Difference between genotypes was statistically not significant. n=5-9/timepoint. **j**) Flow cytometric analysis of tissue resident (TRAMs) and infiltrating monocyte-derived alveolar macrophages (MoAMs) out of the total lung CD45+ cell population normalized to body weight during the IAV response, n=4/timepoint. **k)** Levels of inflammatory cytokines in BALF were assessed using a custom multiplex ELISA. n=3-4/timepoint. Bar graphs represent mean, error bars represent SD, differences between genotypes on each day were assessed by t-test. * p<0.05, ** p<0.001, *** p<0.0001, **** p<0.00001.

Supplemental Figure 1

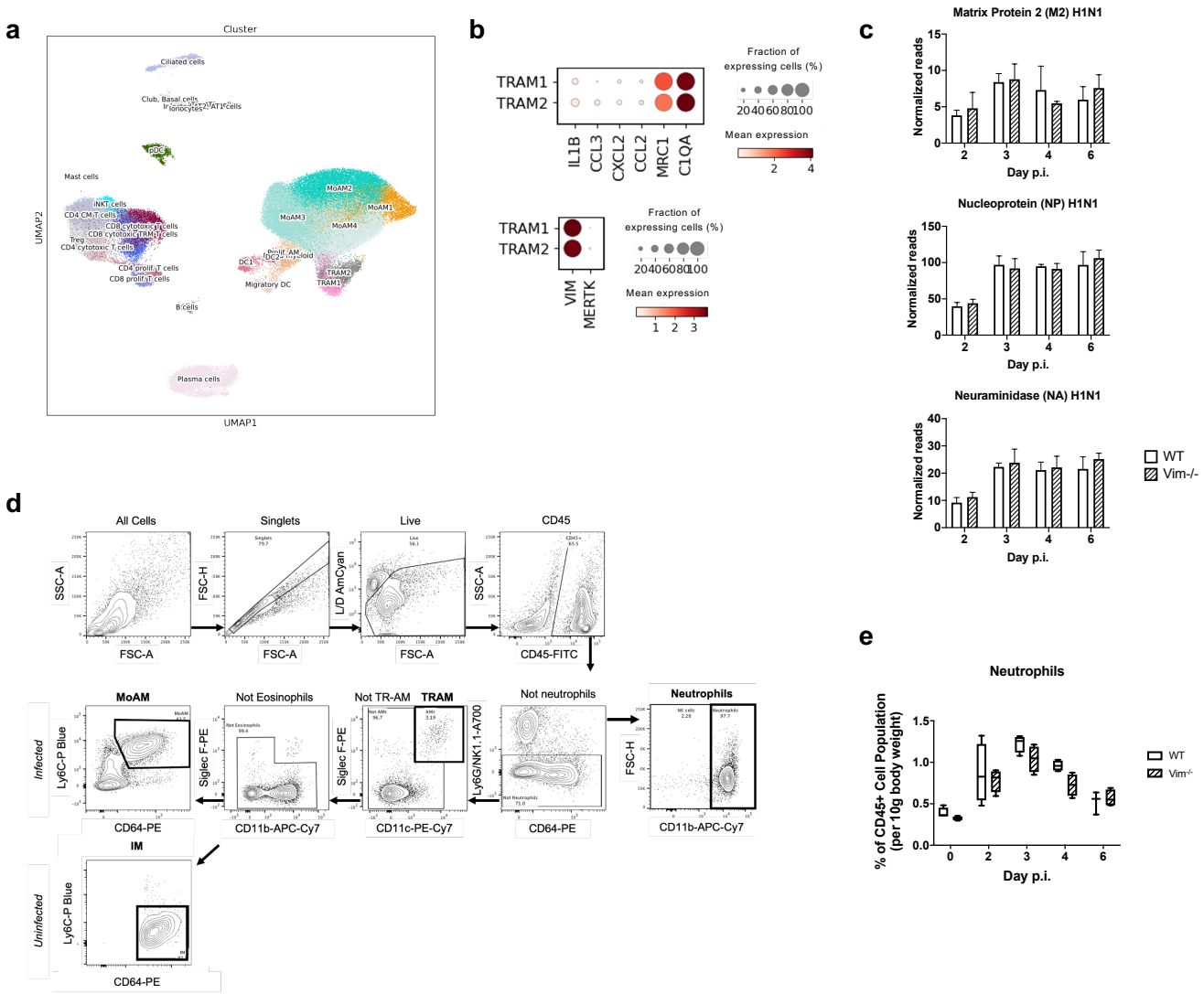

Supplemental Figure 1. **a**) UMAP of 77,146 cells annotated by cell type obtained from 10 patients with severe COVID-19 disease within 48 hours after intubation. **b)** Fraction of cells expressing the representative genes and their mean expression in each TRAM cluster. **c)** Quantification of H1N1 viral RNA molecules detected among RNA isolated from MoAMs, normalized to the number of reads uniquely aligned to mouse genome (mm10) for each sample. Bar graphs represent mean, error bars represent SD. **d)** Gating strategy used for flow cytometry analysis of neutrophils, TRAMs, interstitial macrophages (IM) and MoAMs. **e**) Flow cytometric analysis demonstrated no differences in number of neutrophils out of the total lung CD45+ cell population normalized to body weight between *Vim*$^{-/-}$ and WT mice during the IAV response.

143 alveolar-capillary barrier (**Figure 1f-g**). Histopathological examination of IAV-infected *Vim*-
144 $^{/-}$ mice lungs also demonstrated less severe alveolar damage, characterized by reduced
145 alveolar edema and lower lung tissue damage than in IAV-infected WT mice (**Figure 1h**).
146 Vimentin-deficiency did not interfere with IAV replication or clearance, as evidenced by
147 comparable viral titers (**Figure 1i**) and similar levels of the H1N1 viral RNA molecules, such
148 as matrix protein 2, nucleoprotein, and neuraminidase, which were detected in
149 macrophages from WT and *Vim*$^{-/-}$ mice by RNA-seq (**Supplemental Figure 1c**). These
150 results indicate that *Vim*$^{-/-}$ mice have decreased lung injury and improved survival rates
151 following IAV infection independent of viral load.
152
153 The influx of immune cells into the airspace during IAV infection and the resulting
154 production of pro-inflammatory cytokines is a major driver of lung injury. To characterize
155 the immune cell recruitment into the lungs, we performed a systematic flow cytometric
156 analysis of whole-lung lysates (**Supplemental figure 1d**). The number of TRAMs rapidly
157 decreased after IAV infection at a similar rate in both genotypes, with a more than 80%
158 reduction by 6 days p.i. (**Figure 1j**). MoAMs were deficient in the alveolar compartment at
159 steady-state (e.g., 0 days p.i.) and recruited into the lung parenchyma following infection
160 with IAV[6]. WT and *Vim*$^{-/-}$ IAV infected lungs recruited comparably increasing numbers of
161 MoAMs from 2 days p.i. onward (**Figure 1j**). Similarly, neutrophils peaked on day 3 p.i. in
162 both genotypes (**Supplemental Figure 1e**). Despite similar immune cell recruitment, *Vim*-
163 $^{/-}$ mice had decreased levels of pro-inflammatory cytokines and chemokines, such as IL-
164 1β, TNFα, RANTES, MIP-2, MCP-1, and Type I interferons IFNα/β, compared to WT mice
165 following IAV infection (**Figure 1k**). In summary, wild-type mice, but not *Vim*$^{-/-}$ mice,

166 exhibited a hyperinflammatory phenotype in response to IAV. As there was no difference
167 in MoAM recruitment between genotypes, these data implicate a vimentin-dependent
168 change in MoAM function.
169
170 **Three distinct temporal patterns characterize the transcriptional response of MoAMs**
171 **to influenza A virus**
172 To investigate the response of WT MoAMs to IAV infection, we performed RNA-seq on
173 flow-sorted MoAMs to assess global gene expression profiles on 2, 3, 4, and 6 days post-
174 IAV infection (**Supplemental Figure 2a, 2b**). We identified 2623 differentially expressed
175 genes over this time course and, using k-means clustering, defined three clusters that
176 correspond temporally to three phases of the IAV response: Infiltrating (2 days p.i.), Early
177 Inflammatory (3-4 days p.i.), and Late Inflammatory (6 days p.i.) (**Figure 2a**).
178
179 The first cluster is characterized by genes with the highest expression in the **Infiltrating**
180 **Phase** at 2 days p.i. (**Figure 2a-b, Supplemental Figure 2c**). Through Gene Ontology
181 (GO) analysis, we find this cluster is enriched for genes associated with *cell migration* and
182 *cell adhesion*, such as *Cx3cr1, Rock1, Tln1, and Cxcl14* (**Figure 2c-d**), likely involved in
183 transendothelial migration of leukocytes[21-24]. These results are consistent with the
184 requirement for MoAMs to leave the vasculature and migrate across the endothelium to
185 reach the alveolar space soon after IAV infection. We also observed genes in this cluster
186 associated with the recruitment of lymphocytes, such as *Cd86,* MHC Class II gene *H2-Aa,*
187 and *Ccl8* (**Figure 2c,d, Supplemental Figure 2d**). Furthermore, our results suggest that
188 MoAM may be proliferating during this phase due to the enrichment of GO processes, such

Figure 2

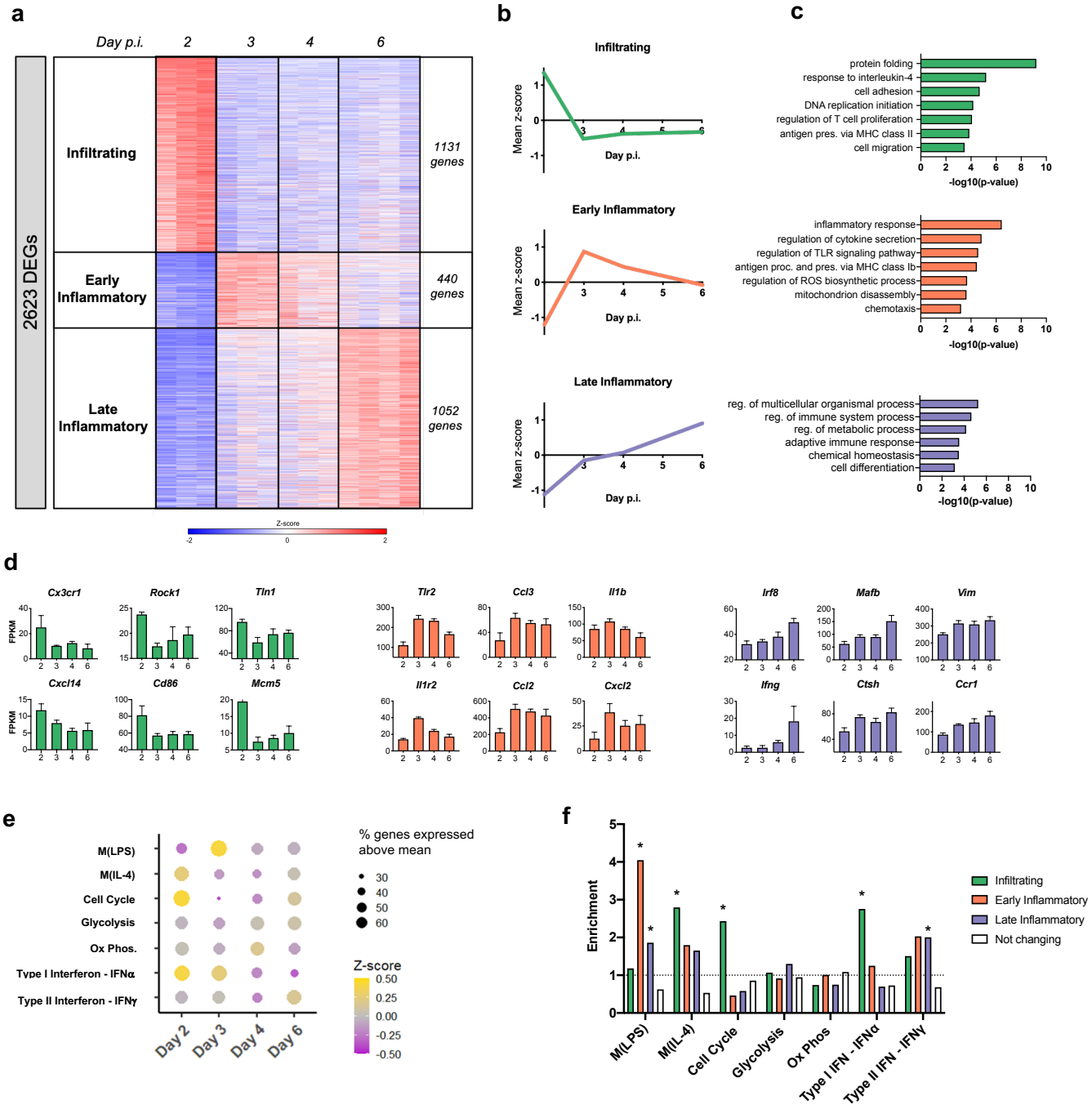
a
Day p.i.
2
3
4
6
2623 DEGs
Infiltrating
Early Inflammatory
Late Inflammatory
1131 genes
440 genes
1052 genes
Z-score
-2
0
2
b
Infiltrating
Early Inflammatory
Late Inflammatory
Mean z-score
Day p.i.
c
protein folding
response to interleukin-4
cell adhesion
DNA replication initiation
regulation of T cell proliferation
antigen pres. via MHC class II
cell migration
inflammatory response
regulation of cytokine secretion
regulation of TLR signaling pathway
antigen proc. and pres. via MHC class Ib
regulation of ROS biosynthetic process
mitochondrion disassembly
chemotaxis
reg. of multicellular organismal process
reg. of immune system process
reg. of metabolic process
adaptive immune response
chemical homeostasis
cell differentiation
-log10(p-value)
d
Cx3cr1
Rock1
Tln1
Tlr2
Ccl3
Il1b
Irf8
Mafb
Vim
Cxcl14
Cd86
Mcm5
Il1r2
Ccl2
Cxcl2
Ifng
Ctsh
Ccr1
FPKM
e
M(LPS)
M(IL-4)
Cell Cycle
Glycolysis
Ox Phos.
Type I Interferon - IFNα
Type II Interferon - IFNγ
Day 2
Day 3
Day 4
Day 6
% genes expressed above mean
30
40
50
60
Z-score
0.50
0.25
0.00
-0.25
-0.50
f
Enrichment
Infiltrating
Early Inflammatory
Late Inflammatory
Not changing
M(LPS)
M(IL-4)
Cell Cycle
Glycolysis
Ox Phos
Type I IFN - IFNα
Type II IFN - IFNγ

Figure 2. Wild-type monocyte-derived alveolar macrophages exhibit gene expression patterns associated with three phases of influenza A viral infection. a) Heatmap of normalized expression of 2,623 differentially expressed genes (ANOVA adjusted p-value <0.05). Z-score normalization for each row was applied to gene expression (FPKM) data. K-means clustering (k=3) identified three clusters; Infiltrating (1131 genes), Early Inflammatory (440 genes), Late Inflammatory (1052 genes). **b)** Mean z-scores calculated across genes for each cluster **c)** Gene Ontology (GO) term enrichment for each phase. **d)** Bar graphs of gene expression (FPKM) for representative genes in each phase. Error bars represent SD. (ANOVA adjusted p-value <0.05). **e)** Bubble plot representing the proportion of genes (%) within each process that had an expression above the row mean. Color gradient represents mean z-score of expression across genes. **f)** Enrichment of gene sets in each cluster as defined in A. Asterisk represents significantly enriched overlaps (hypergeometric p-value <0.0018, FWER = 0.05). Dotted line indicates expected enrichment score of 1. n=3-4 per group. Ox Phos = Oxidative phosphorylation.

Supplemental Figure 2

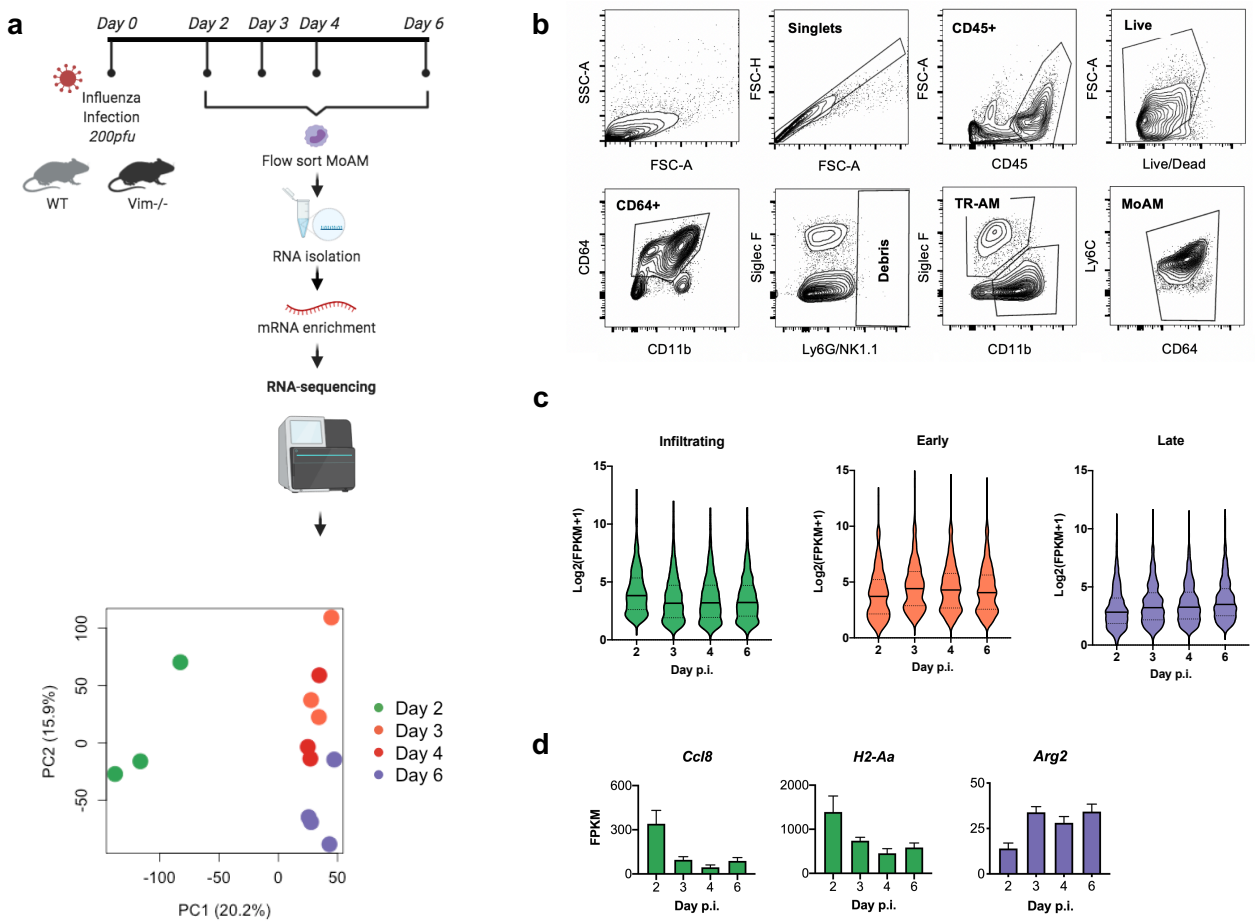

Supplemental Figure 2. a) Schematic of experimental design and workflow. WT or *Vim*$^{-/-}$ mice were infected with a lethal dose of influenza A virus (200 pfu). MoAMs were sorted by flow cytometry (FACS) from lungs on 2, 3, 4, and 6 days p.i. Total RNA was isolated, mRNA was enriched, and bulk RNA-seq was performed. Principal component analysis (PCA) was used to visualize replicates. **b)** Sequential gating strategy used for FACS collection of TRAMs and MoAMs **c)** Violin plots of $\log_2$(FPKM+1) counts data for all genes in each cluster. Solid lines represent median, dotted lines represent quartiles. **d)** Bar graphs of gene expression (FPKM) in MoAM for representative genes in each phase. Error bars represent SD. (ANOVA adjusted p-value <0.05).

189 as *DNA replication initiation*, and the expression of cell cycle genes, such as *Mcm5*, in this
190 cluster (**Figures 2c-f**). Taken together, these data show that the primary role of MoAMs in
191 the Infiltrating Phase of the IAV response is to enter the lung parenchyma and promote the
192 recruitment of immune cells.
193
194 The second cluster is characterized by genes that peak in expression during the **Early**
195 **Inflammatory Phase** at 3 days p.i. (**Figure 2a-b, Supplemental Figure 2c**). This cluster
196 is enriched for genes associated with *inflammatory response* and *regulation of cytokine*
197 *secretion* (**Figure 2c)** – such as *Tlr2*, *Il1b,* and *Il1r2* **(Figure 2d)**. These gene expression
198 changes correspond with the secretion of inflammatory cytokines, such as IL-1β and TNFα,
199 beginning on Day 3 of IAV response (**Figure 1k)** and binding of viral PAMPs through pattern
200 recognition receptors (PRRs), including TLR2[25]. The expression of genes associated with
201 *chemotaxis,* such as *Ccl3, Ccl2,* and *Cxcl2,* also peak during the Early Inflammatory phase
202 (**Figure 2c-d**) and corresponds with the secretion of their respective proteins MCP-1, MIP1-
203 α and MIP-2 measured in the BALF (**Figure 1k**). These data collectively suggest that WT
204 MoAMs adopt a pro-inflammatory state during the Early Inflammatory Phase of the IAV
205 response.

206 The third cluster is characterized by genes that display a continuous increase in expression
207 until the **Late Inflammatory Phase** at 6 days p.i. (**Figure 2a-b, Supplemental Figure 2c**).
208 This cluster is enriched for genes associated with the GO processes of *cell differentiation*
209 and *adaptive immune response* – such as *Irf8, Mafb, Ifng, Ctsh, Ccr1* and*, Arg2* (**Figure**
210 **2d, Supplemental Figure 2d).** The increasing expression of *Irf8* and *Mafb* are in line with
211 the transition from a monocyte to macrophage-like state[26]. Although GO analysis implicated

212 metabolic processes in this cluster (**Figure 2c**), and macrophage activation has been
213 associated with cellular respiration changes[27-29], we did not observe preferential expression
214 of genes in the glycolysis or oxidative phosphorylation pathways at any time point (**Figure**
215 **2e-f**). Interestingly, the gene encoding vimentin increased in expression over the time
216 course, suggesting that vimentin may play a role throughout the IAV response (**Figure 2d**).
217 Overall, these data suggest that WT MoAMs initiate a shift to a more adaptive immune
218 response by the Late Inflammatory phase.

219

220 Since interferon pathways are an essential element of the viral immune response, we
221 investigated Type I and Type II interferon genes' temporal expression. We found Type I
222 *IFN*α response genes peaked in expression on day 2, which coincided with their
223 enrichment in the Infiltrating cluster (**Figure 2e-f)**. In contrast, Type II *IFNy* response genes
224 did not reach their highest expression level until 6 days p.i. and were enriched in the Late
225 Inflammatory cluster (**Figure 2e-f)**. This data supports Type I interferon's role as an early
226 effector of the immune response, while Type II interferon is involved in the later adaptive
227 immune response.

228

229 While GO analysis can be informative, many of the terms, such as *inflammatory response*
230 and *innate immune response,* lack cell-type-specificity. We took advantage of published
231 studies of *in vitro* stimulated MoAMs, polarized towards a pro-inflammatory or alternatively-
232 activated phenotype through the administration of LPS or IL-4, respectively[30-33]. To
233 determine whether similar states were observed during our IAV time course, we generated

234 annotations for these responses by integrating the gene sets resulting from several
235 published studies on LPS ($M_{(LPS)}$) and IL-4 ($M_{(IL-4)}$) stimulation in macrophages (see
236 Methods). We found that $M_{(IL-4)}$ genes peaked on day 2 p.i. and were enriched in the
237 Infiltrating cluster (**Figure 2e-f)**. Furthermore, we found that t $M_{(LPS)}$ genes peaked on day
238 3 p.i. in WT MoAMs **(Figure 2e**) and were enriched in the Early Inflammatory cluster
239 (**Figure 2f**). $M_{(LPS)}$ genes were also enriched to a lesser degree in the Late Inflammatory
240 cluster (**Figure 2f**). It is worth noting that although we observe these general trends, the *in*
241 *vivo* state of MoAMs does not entirely reflect the responses defined by our *in vitro* derived
242 annotated gene lists. Taken together, our results support a critical switch in WT MoAM
243 function as they transition from their initial transcriptional state in the Infiltrating phase to a
244 more pro-inflammatory phenotype during the Early and Late Inflammatory phases.
245
246 At least two phenotypically distinct macrophages are present in the lung at steady-state:
247 TRAMs and interstitial macrophages (IMs). In steady-state conditions, IMs are found at
248 two-fold lower frequencies than TRAMs in mouse lung tissue[34]. Interstitial macrophage
249 numbers expand more rapidly in response to PAMPs and DAMPs compared with
250 TRAMs[34], and are preferentially replenished from blood monocytes compared with
251 TRAMs[35]. To determine whether MoAMs resembled steady-state lung macrophages
252 during the response to IAV, we defined TRAM- and IM-specific gene sets by performing
253 RNA-seq on flow-sorted TRAM and IM cells from uninfected WT animals (**Figure 3a).** We
254 observed that WT MoAMs decrease expression of IM-specific genes over the course of IAV
255 infection, while they increase expression TRAM-specific genes (**Fig 3b,c**). For example,
256 *Cx3cr1* and *Lyve1* exhibit highest expression on day 2 p.i., while *Il17ra* and *Csf2rb*

Figure 3

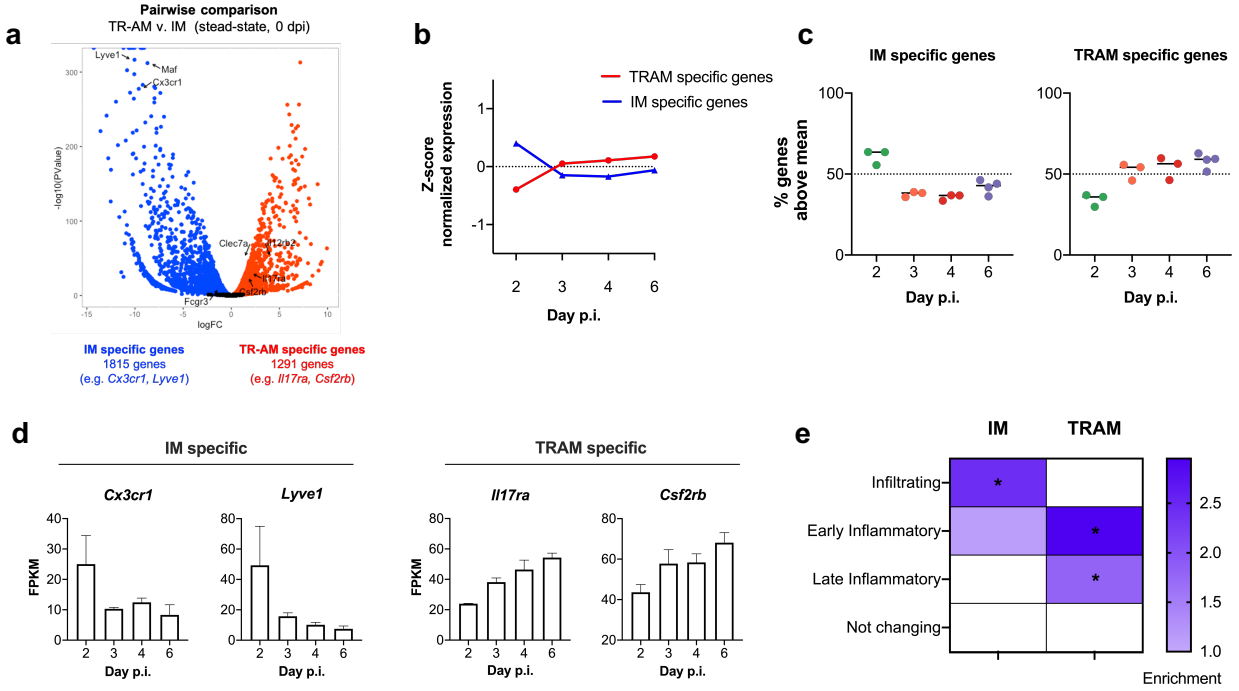

Figure 3. Wild-type monocyte-derived alveolar macrophages resemble interstitial macrophages during the infiltrating phase and exhibit increased expression of alveolar macrophages genes over time. a) Volcano plot of differentially expressed genes (edgeR p-value<0.05, and edgeR reported log2FC>|1.0|) between TRAM and IM at steady-state (0 dpi). The number of genes increased (red) and decreased (blue) in TRAMs compared to IMs are shown. **b)** Mean z-scores calculated for IM- and TRAM-specific gene sets over the course of IAV infection in MoAMs **c)** Plots representing % of genes at each time point expressed above the mean. Each dot represents a replicate. Lines represent median. **d)** Bar graphs of gene expression (FPKM) for representative genes in IM- and TRAM-specific gene sets. Error bars represent SD. **e)** Enrichment of IM- and TRAM-cell specific gene signatures in MoAMs for each phase. Asterisk represents significantly enriched overlaps (hypergeometric p-value <0.006, FWER = 0.05).

257 progressively increase in expression until day 6 p.i. (**Figure 3d**). Similarly, the IM gene
258 signature is significantly enriched in the Infiltrating phase, whereas and the TRAM gene
259 signature is significantly enriched in both the Early and Late Inflammatory clusters (**Figure**
260 **3e)***.* These data suggest that WT MoAMs resemble steady-state IMs transcriptionally upon
261 extravasation, but become more like steady-state TRAMs as IAV infection progresses.
262
263 ***Vim*$^{-/-}$ MoAMs exhibit increased expression of Infiltrating phase genes and decreased**
264 **expression of Early Inflammatory phase genes**
265
266 To gain a better understanding of the conferred protection from IAV infection in *Vim*$^{-/-}$ mice
267 (**Figure 1**), we performed RNA-seq on flow-sorted MoAMs from *Vim*$^{-/-}$ mice at days 2, 3, 4,
268 and 6 following IAV infection (**Supplemental Figures 2a, 2b, 4a**). Using the prior clustering
269 of 2623 genes across the three phases of the IAV response (**Figure 2a**), we compared
270 expression between MoAMs in WT and *Vim*$^{-/-}$ mice (**Figure 4a**). While *Vim*$^{-/-}$ MoAMs
271 exhibited the same overall gene expression patterns, we found that genes in the Infiltrating
272 cluster tended to be increased in expression while genes in the Early Inflammatory cluster
273 tended to be decreased (**Figure 4b-d, Supplemental Figure 4b**). In contrast, genes in the
274 Late Inflammatory cluster were less changed between genotypes (**Figure 4b-d,**
275 **Supplemental Figure 4b**). Interestingly, day 3 p.i. represented the largest difference
276 between genotypes in any cluster. In line with these observations, day 2 and day 3 *Vim*$^{-/-}$
277 MoAMs were globally more similar to each other than their WT counterparts, and the
278 change in expression associated with the transition from 2 to 3 days p.i. was reduced
279 (**Supplemental Figure 4c,d)**. Steady-state *Vim*$^{-/-}$ TRAM and IM gene expression from
280 uninfected mice were mostly unchanged from WT cells, suggesting that vimentin-deficiency

Figure 4

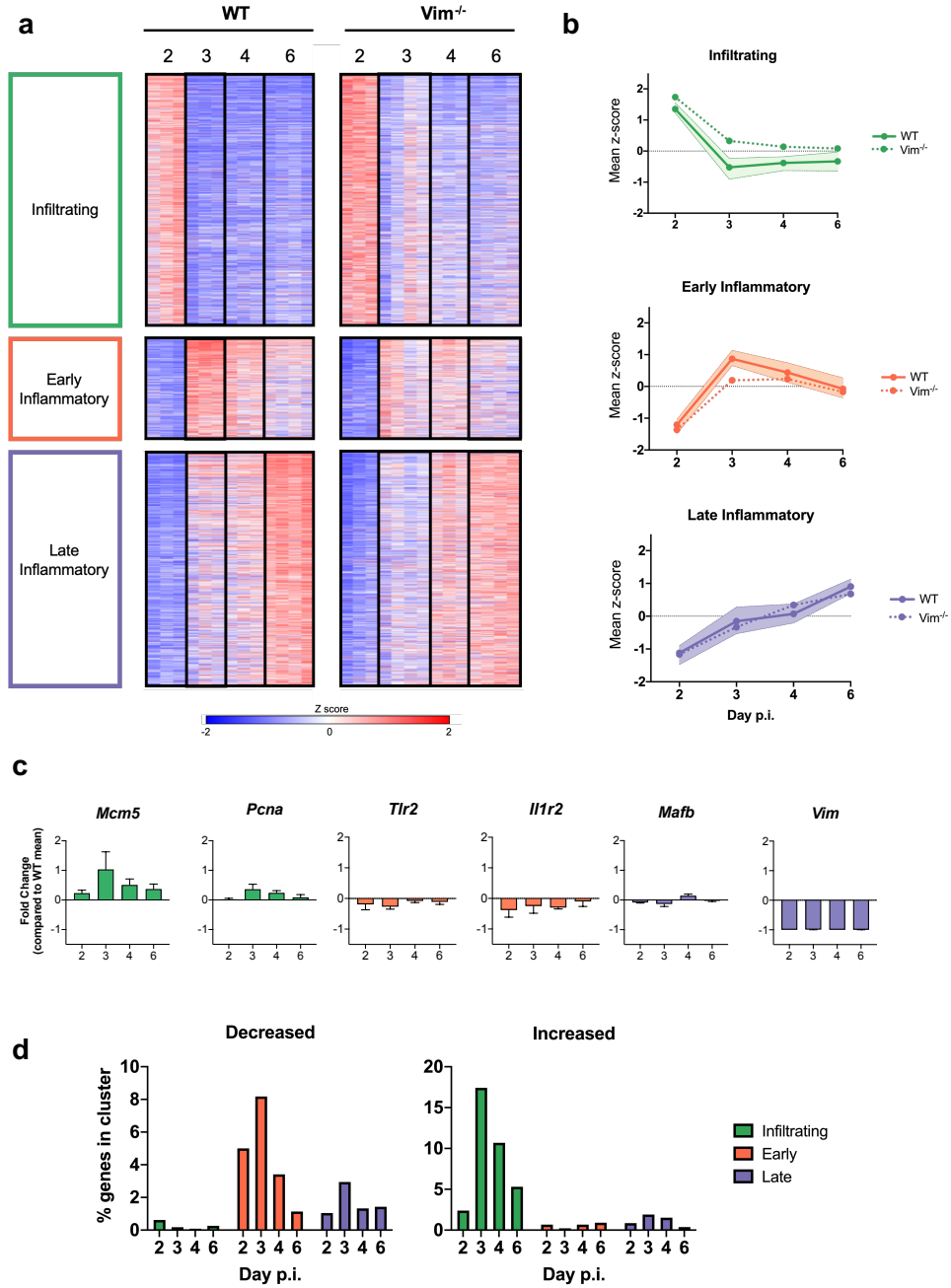

Figure 4. *Vim-/-* MoAMs exhibit increased expression of Infiltrating phase genes and decreased expression of Early Inflammatory phase genes. a) Heatmap of normalized expression of 2,623 genes as defined in Figure 2a. *Vim*$^{-/-}$ data was normalized to the WT mean and standard deviation (adapted z-score). **b**) Mean adapted z-scores were calculated across genes for each cluster in WT MoAMs and *Vim*$^{-/-}$ MoAMs. Shading represents WT MoAMs inter-quartile range (IQR) **c**) Bar graphs representing the fold change in gene expression (FPKM) in *Vim*$^{-/-}$ MoAMs compared to the WT MoAMs mean for representative genes. (n=3-4 per group). **d)** % genes in each cluster that exhibit decreased or increased expression in *Vim*$^{-/-}$ MoAMs compared to WT MoAMs (n=3-4 per group). Decreased genes defined as $\log_2 FC < -0.58$ (FC of 1.5); increased genes defined as $\log_2 FC > 0.58$.

Supplemental Figure 4

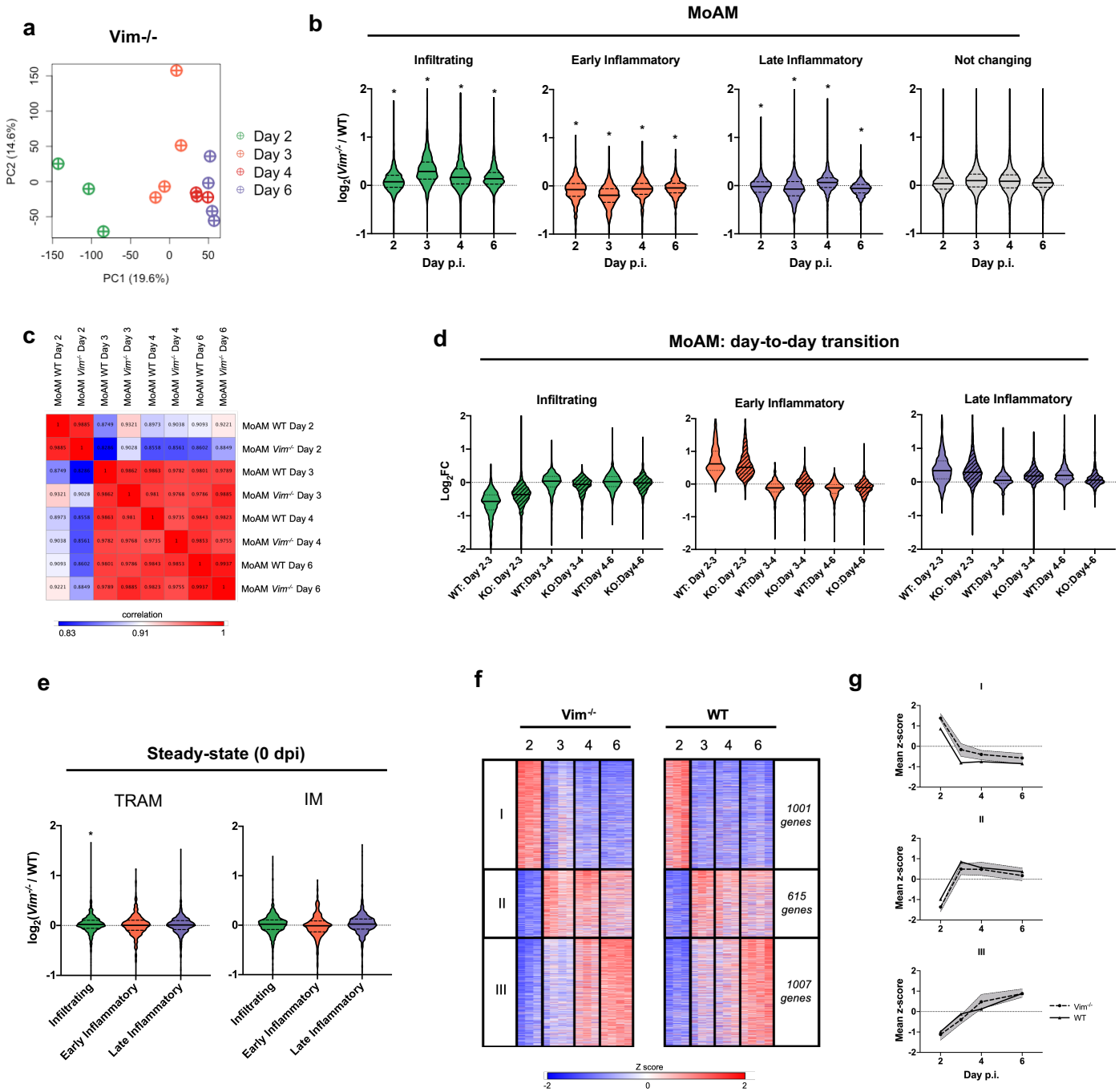

Supplemental Figure 4. a) Principal component analysis (PCA) of *Vim*$^{-/-}$ MoAMs replicates. **b)** Violin plots representing the $\log_2$FC between *Vim*$^{-/-}$ and WT for each gene by cluster in MoAMs. Solid lines represent median, dotted lines represent quartiles. **c)** Heatmap showing pairwise Pearson correlation of mean gene expression across replicates between each time point in WT and *Vim*$^{-/-}$ MoAMs. Pearson correlation coefficient values shown within each square. Scale bar represents Pearson correlation coefficient. **d)** Violin plots representing the $\log_2$FC between days p.i. for each gene by cluster in WT and *Vim*$^{-/-}$ MoAMs. Solid lines represent median, dotted lines represent quartiles. **e)** Violin plots representing the $\log_2$FC between *Vim*$^{-/-}$ and WT in TRAMs and IMs at steady-state (0 dpi) for each gene by cluster. Solid lines represent median, dotted lines represent quartiles. **f)** Heatmap of normalized expression of 2,623 differentially expressed genes in *Vim*$^{-/-}$ MoAMs (ANOVA adjusted p-value <0.05). Adapted Z-score normalization for each row was applied to gene expression (FPKM) data using *Vim*$^{-/-}$ MoAMs mean and standard deviation. K-means clustering (k=3) was performed on *Vim*$^{-/-}$ MoAMs expression and WT MoAMs data was visualized for the same genes **g**) Mean adapted z-scores were calculated across genes for each cluster in *Vim*$^{-/-}$ and WT MoAMs. Shading represents *Vim*$^{-/-}$ MoAMs IQR.

281 has a larger effect during the response to IAV-infection than in steady-state (**Supplemental**
282 **Figure 4e**).
283
284 Additionally, we performed a reverse analysis where we first clustered on differentially
285 expressed genes across IAV infection in *Vim*$^{-/-}$ MoAMs and then compared with the
286 expression of these 2623 genes in WT MoAMs (**Supplemental Figure 4f,g)**. Although the
287 gene sets did not entirely overlap, the resulting gene expression patterns were generally
288 conserved, and no new GO processes were identified. These results support an altered
289 function of *Vim*$^{-/-}$ MoAMs in response to IAV that favors the maintenance of Infiltrating phase
290 genes and the suppression of Early Inflammatory phase genes to confer protection from
291 influenza-induced lung injury.
292
293 **Identification of cellular processes impacted in *Vim*$^{-/-}$ MoAMs response to IAV.**
294 To further investigate the pathways influenced by vimentin-deficiency in IAV infection, we
295 evaluated global gene expression between genotypes on each day p.i. (**Figure 5a).**
296 Compared to WT MoAMs, we found that *Vim*$^{-/-}$ MoAMs exhibit decreased expression of
297 genes involved in the inflammatory response and stress response throughout IAV infection
298 and increased expression of genes involved in cell cycle and extracellular matrix
299 organization (**Figure 5b)**. Furthermore, we found that gene sets associated with
300 inflammation – including M(LPS), Type I Interferon, and Type II Interferon – were
301 significantly decreased in expression in *Vim*$^{-/-}$ MoAMs on every day p.i.; however, these
302 responses peaked at different days of IAV infection in wild-type mice (**Figure 5c,**
303 **Supplemental Figure 5a-c)**. In contrast, *Cell Cycle* and *M(IL-4)* associated genes were

Figure 5

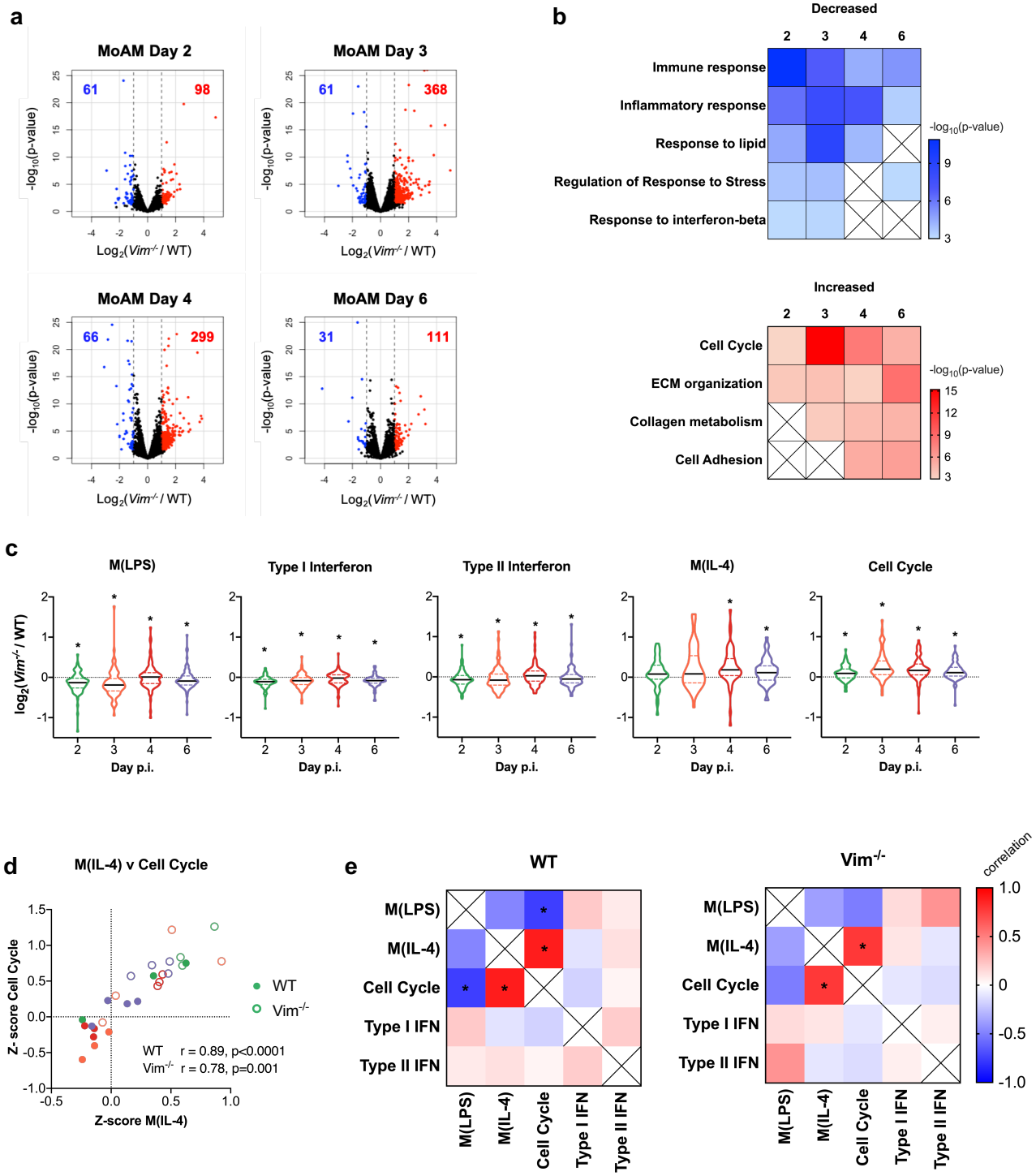
a
MoAM Day 2
61
98
MoAM Day 3
61
368
MoAM Day 4
66
299
MoAM Day 6
31
111
-log10(p-value)
Log2(Vim-/- / WT)
b
Decreased
2 3 4 6
Immune response
Inflammatory response
Response to lipid
Regulation of Response to Stress
Response to interferon-beta
-log10(p-value)
Increased
Cell Cycle
ECM organization
Collagen metabolism
Cell Adhesion
c
M(LPS)
Type I Interferon
Type II Interferon
M(IL-4)
Cell Cycle
log2(Vim-/- / WT)
Day p.i.
d
M(IL-4) v Cell Cycle
Z- score Cell Cycle
Z-score M(IL-4)
WT
Vim-/-
WT r = 0.89, p<0.0001
Vim-/- r = 0.78, p=0.001
e
WT
Vim-/-
M(LPS)
M(IL-4)
Cell Cycle
Type I IFN
Type II IFN
correlation

Figure 5. Inflammatory pathways are consistently decreased in *Vim*$^{-/-}$ MoAMs compared to WT MoAMs during influenza A infection. **a)** Volcano plots of differentially expressed genes (edgeR p-value<0.05, and edgeR reported $\log_2$FC>|1.0|) between *Vim*$^{-/-}$ and WT MoAMs on each day post-infection. The number of genes increased (red) and decreased (blue) in *Vim*$^{-/-}$ compared to WT MoAMs are shown. **b)** GO term enrichment across days p.i. in the increased (red) and decreased (blue) genes in *Vim*$^{-/-}$ compared to WT MoAMs. Scale represents -$\log_{10}$ p-value. **c)** Violin plots representing the $\log_2$FC for each process between *Vim*$^{-/-}$ and WT MoAMs. Solid lines represent median, dotted lines represent quartiles. **d)** Scatter plots of z-score normalized gene expression across genes in $M_{(IL\text{-}4)}$ vs Cell Cycle. Pearson correlation coefficients (r) across WT or *Vim*$^{-/-}$ MoAM replicates and associated p-values are shown. **e)** Heatmap matrix of Pearson correlation between processes, asterisk indicate p-value <0.05.

Supplemental Figure 5

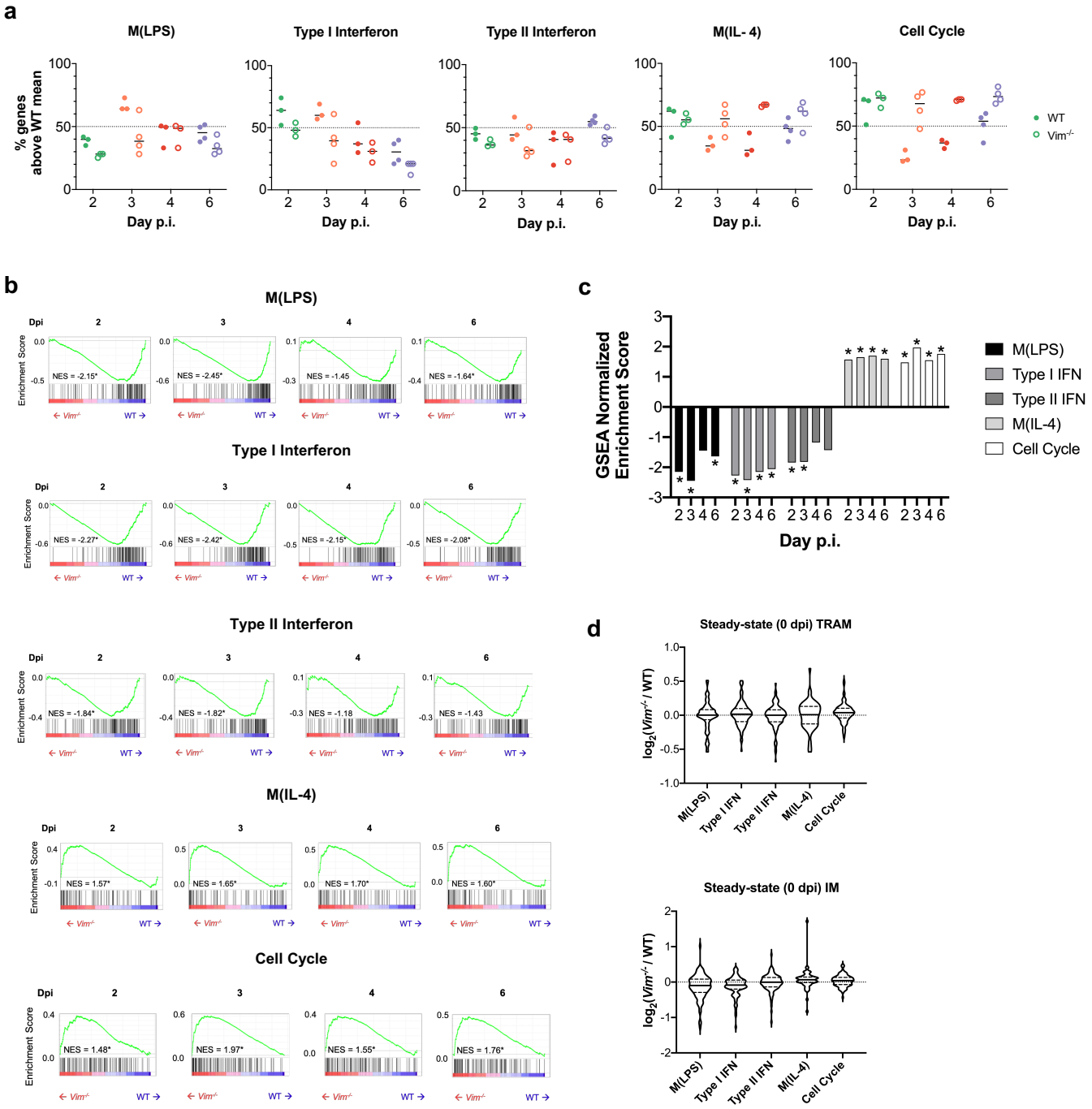

Supplemental Figure 5. a) Plots representing % of genes at each time point expressed above their WT mean. Each dot represents a replicate. Lines represent median. **b, c)** Gene Set Enrichment Analysis (GSEA) enrichment plots. GSEA was performed on gene lists ranked by edgeR reported fold-change between *Vim*$^{-/-}$ and WT MoAMs at each time point. Normalized enrichment scores (NES) are shown. Asterisks indicate statistically significant adjusted p-values <0.05. **d)** Violin plots representing the $\log_2$FC between *Vim*$^{-/-}$ and WT TRAMs and IMs at steady-state (0 dpi). Solid lines represent medians, dashed lines represent quartiles.

304 increased in expression in *Vim*$^{-/-}$ MoAMs compared to WT MoAMs (**Figure 5c,**
305 **Supplemental Figure 5a-c**). In this case, the difference in expression between genotypes
306 appears to be driven by the failure of *Vim*$^{-/-}$ MoAMs to reduce the expression of *Cell*
307 *Cycle* and *M(IL-4)* associated genes during the course of IAV infection as observed in WT
308 mice. None of these gene sets were significantly different in expression in steady-state
309 alveolar macrophages (TRAMs and IMs) **Supplemental Figure 5d**).
310
311 We next asked whether any of the individual gene sets correlated with each other. We
312 observed that $M_{(IL\text{-}4)}$ and Cell cycle gene expression are highly correlated in both
313 genotypes, suggesting they may be part of a more extensive network of co-regulated
314 processes (**Figure 5d-e**). Taken together, these data suggest that MoAM activation
315 following IAV infection is affected by the loss of vimentin through the precise temporal
316 regulation of specific pathways.
317
318 ***Vim*$^{-/-}$ MoAMs fail to activate core pro-inflammatory genes in the early response to**
319 **IAV**
320 Thus far, our results suggest that the suppression of pro-inflammatory genes across IAV
321 infection, particularly in the Early Inflammatory phase, is responsible for the protection
322 conferred by vimentin-deficiency. To identify specific genes involved in this process, we
323 focused on the $M_{(LPS)}$ response, which was associated with an increased expression on
324 day 3 p.i. in WT mice. In MoAMs from *Vim*$^{-/-}$ mice, fewer $M_{(LPS)}$ genes exhibited peak
325 expression on day 3 p.i. (**Figure 6a**). Moreover, $M_{(LPS)}$ genes were enriched among those
326 genes exhibiting the greatest expression decrease in *Vim*$^{-/-}$ MoAMs compared with WT

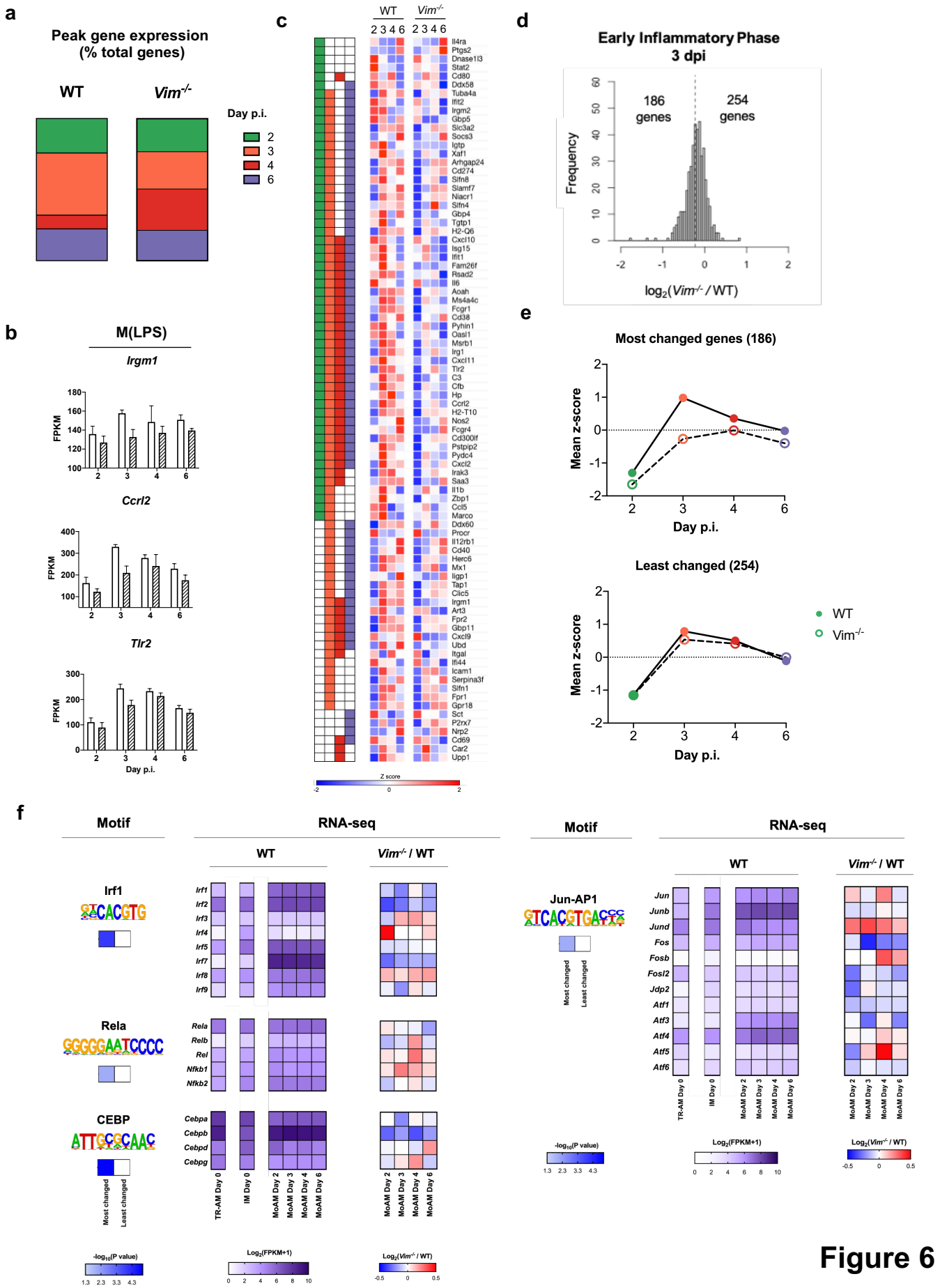
a
Peak gene expression
(% total genes)
WT
Vim-/-
Day p.i.
2
3
4
6
b
M(LPS)
Irgm1
Ccrl2
Tlr2
FPKM
Day p.i.
c
WT
Vim-/-
2 3 4 6
2 3 4 6
Il4ra
Ptgs2
Dnase1l3
Stat2
Cd80
Ddx58
Tuba4a
Ifit2
Irgm2
Gbp5
Slc3a2
Socs3
Igtp
Xaf1
Arhgap24
Cd274
Sifn8
Slamf7
Niacr1
Sifn4
Gbp4
Tgtp1
H2-Q6
Cxcl10
Isg15
Ifit1
Fam26f
Rsad2
Il6
Aoah
Ms4a4c
Fcgr1
Cd38
Pyhin1
Oasl1
Msrb1
Irg1
Cxcl11
Tlr2
C3
Cfb
Hp
Ccrl2
H2-T10
Nos2
Fcgr4
Cd300lf
Pstpip2
Pydc4
Cxcl2
Irak3
Saa3
Il1b
Zbp1
Ccl5
Marco
Ddx60
Procr
Il12rb1
Cd40
Herc6
Mx1
Iigp1
Tap1
Clic5
Irgm1
Art3
Fpr2
Gbp11
Cxcl9
Ubd
Itgal
Ifi44
Icam1
Serpina3f
Sifn1
Fpr1
Gpr18
Sct
P2rx7
Nrp2
Cd69
Car2
Upp1
Z score
d
Early Inflammatory Phase
3 dpi
186
genes
254
genes
Frequency
log2(Vim-/- / WT)
e
Most changed genes (186)
Least changed (254)
Mean z-score
Day p.i.
WT
Vim-/-
f
Motif
RNA-seq
WT
Vim-/- / WT
Irf1
Rela
CEBP
Jun-AP1
Most changed
Least changed
TR-AM Day 0
IM Day 0
MoAM Day 2
MoAM Day 3
MoAM Day 4
MoAM Day 6
-log10(P value)
Log2(FPKM+1)
Log2(Vim-/- / WT)

Figure 6

Figure 6. Protective phenotype of *Vim*$^{-/-}$mice is associated with the failure of *Vim*$^{-/-}$MoAMs to activate core pro-inflammatory genes in the early response to IAV. a) Percent (%) $M_{(LPS)}$ genes peaking in expression on each day post-infection in WT and *Vim*$^{-/-}$ MoAMs **b)** Bar graphs of gene expression (FPKM) for representative $M_{(LPS)}$ genes present in the leading edge of at least 1 day from GSEA. Error bars represent SD. **c)** Heatmap of normalized expression of 84 $M_{(LPS)}$ genes present in the GSEA leading edge on at least 1 day (indicated by color-coded bar on left). Adapted Z-score normalization using WT mean and standard deviation for each row was applied to gene expression (FPKM) data. **d)** Histogram representing the distribution of $\log_2$FC between *Vim*$^{-/-}$ and WT MoAMs on 3 dpi of the Early Inflammatory phase (440 genes). Dashed line represents mean of the distribution. Number of genes less than (186) and greater than (254) the mean are shown. Genes with $\log_2$FC between *Vim*$^{-/-}$ and WT MoAMs less than the mean represent those genes that are most changed between *Vim*$^{-/-}$ and WT MoAMs. **e)** Mean adapted z-scores were calculated across genes for most (186) and least (254) changed genes on 3 dpi in the Early Inflammatory Phase in WT and *Vim*$^{-/-}$ MoAMs. **f)** HOMER known motif analysis using genomic background of most changed genes on 3 dpi in the Early Inflammatory Phase (186 genes). Motif logos are shown below motif names. -$\log_{10}$pvalues of enrichment in most or least changed gene set is shown. Log_2(FPKM+1) average gene expression of transcription factor family members are shown for WT TRAMs and WT IMs at steady-state (0 dpi) and 2-6 dpi for WT MoAMs. $\log_2$FC between *Vim*$^{-/-}$ and WT MoAM gene expression of transcription factor family members on each dpi. (n=3-4)

Supplemental Figure 6

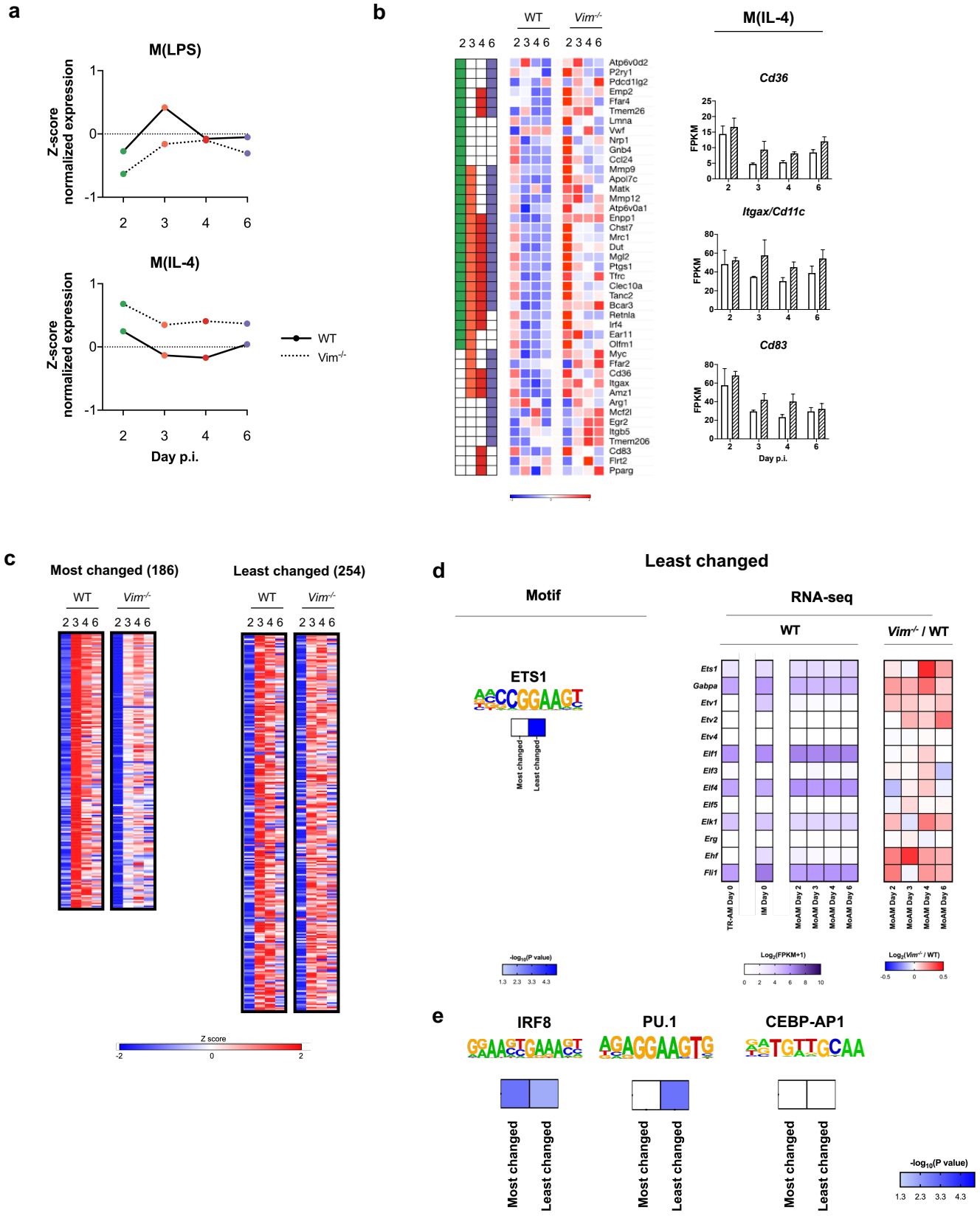

Supplemental Figure 6. a) Mean adapted z-scores for $M_{(LPS)}$ and $M_{(IL\text{-}4)}$ genes present in the leading edge of at least 1 day from GSEA in WT and *Vim*$^{-/-}$ MoAMs. **b)** Heatmap of normalized expression of $M_{(IL\text{-}4)}$ genes present in the leading edge of at least 1 day from GSEA. Adapted Z-score normalization for each row was applied to gene expression (FPKM) data. Bar graphs of gene expression (FPKM) for representative $M_{(IL\text{-}4)}$ genes present in the leading edge of at least 1 day from GSEA. Error bars represent SD. **c)** Heatmap of normalized expression of 186 most changed, and 254 least changed genes on 3dpi of the Early Inflammatory Phase. Adapted Z-score normalization for each row was applied to gene expression (FPKM) data. **d)** HOMER known motif analysis using genomic background of least changed genes on 3 dpi in the Early Inflammatory Phase (254 genes). Motif logos are shown below motif names. Log_2(FPKM+1) average gene expression of transcription factor family members are shown for WT TRAMs and WT IMs at steady-state (0 dpi) and 2-6 dpi for WT MoAMs. log_2FC between *Vim*$^{-/-}$ and WT MoAM gene expression of transcription factor family members on each dpi. (n=3-4). **e)** Motif logos are shown below motif names. -log_{10}pvalues of enrichment in most or least changed gene set is shown.

327 during the course of IAV response (**Supplemental Figure 5b)**. Of the $M_{(LPS)}$ genes that
328 were most decreased on at least one day, we find that the majority failed to intensify in
329 expression on day 3 p.i. in *Vim*$^{-/-}$ MoAM compared with WT MoAM (**Figure 6b-c,**
330 **Supplemental Figure 6a)**. This core set of pro-inflammatory genes includes interferon-
331 stimulated genes (ISGs), such as *Ifit1, Irgm1, and Rsad2*, genes associated with
332 chemokine pathways, including *Ccrl2* and *Cxcl2,* and genes associated with pathogen
333 sensing, *Fcgr1, and Tlr2* (**Figure 6b-c).** In contrast, $M_{(IL-4)}$ genes, such as *Cd36*, *Cd11c,*
334 and *Cd83*, exhibited higher expression on all days post IAV infection in *Vim*$^{-/-}$ MoAMs
335 compared with WT MoAMs (**Supplemental Figures 5b, c, 6b).** Collectively, these data
336 suggest *Vim*$^{-/-}$ MoAMs fail to activate core pro-inflammatory genes associated with the Early
337 Inflammatory phase in response to IAV.
338
339 Prior work has demonstrated that macrophage activation is largely defined by the activity
340 of cell-type-specific transcription factors (TF) that poise regulatory elements for activation
341 by stimulus-specific TFs[36-38]. To better characterize the impact on gene regulation
342 observed in *Vim*$^{-/-}$ MoAMs, we searched for TF binding sites enriched in the promoters of
343 vimentin-dependent genes associated with the Early Inflammatory phase. First, we
344 classified the 440 Early Inflammatory genes into those “most changed” and “least changed”
345 in *Vim*$^{-/-}$ MoAMs based on their fold-change compared with WT MoAMs (**Figure 6d-e,**
346 **Supplemental Figure 6c**). Next, we performed motif-finding on each gene set using a
347 known sequence motifs database (see Methods). We found that TF families previously
348 implicated in an inflammatory response, such as *Jun-AP1* and *Rela*, were significantly
349 enriched among the most changed but not the least changed genes (**Figure 6f**). Some Irf

350 family motifs were differentially enriched between the two gene sets, while others were
351 shared (**Figure 6f**). As supported by induction of gene expression in IAV and the decrease
352 observed in *Vim*$^{-/-}$, those associated with ISGs (*Irf1*/7/9) were more likely to be affected by
353 vimentin-deficiency (**Figure 6f**), while *Irf8*, which is more generally involved in macrophage
354 function, exhibited similar enrichment in both groups (**Supplemental Figure 6e**).
355 Furthermore, the CEBP motif was associated with the most changed genes in *Vim*$^{-/-}$ MoAMs
356 and *Cebpb* was expressed highly at both baseline and throughout IAV infection (**Figure**
357 **6f**). This observation is consistent with *Cebpb*, a known macrophage TF which can also
358 act in combination with AP1 factors (**Figure 6f),** specifying poised regulatory elements in
359 macrophages that activate genes on stimulation[39,40]. On the other hand, ETS was the main
360 TF family with motifs enriched in the least changed but not the most changed genes
361 (**Supplemental Figure 6d**). This family marginally includes PU.1, a well-known myeloid
362 lineage factor, but PU.1 is unlikely to have a specific role in IAV response (**Supplemental**
363 **Figure 6e**). Instead, the expression of *Elf1* and *Elf4* suggests that they may have an
364 interferon-independent antiviral role in influenza as previously reported[41], that is not
365 impacted by vimentin-deficiency. In summary, vimentin-deficiency impedes the stimulus-
366 dependent regulation of pro-inflammatory genes in MoAMs during the Early Inflammatory
367 phase of IAV infection. Although this effect leads to subtle changes in overall gene
368 expression, it appears to be sufficient to alter MoAM function.
369

370 **Vimentin-deficient MoAMs are sufficient to confer protection from IAV-induced**
371 **mortality**

372 To determine whether vimentin-deficiency in recruited macrophages alone decreases lung
373 injury following IAV infection, bone marrow from either WT or *Vim*$^{-/-}$ donor mice (CD45.2)
374 were transferred into irradiated WT recipient mice (CD45.1), allowing for the specific
375 reconstitution of MoAMs with a WT or *Vim*$^{-/-}$ genotype (**Figure 7a**). All mice showed
376 reconstitution of donor hematopoietic cells in peripheral blood above 85% (**Supplementary**
377 **Figure 7a**). Following confirmed engraftment and recovery, mice were infected with a lethal
378 dose of IAV (**Figure 7a**). We found that IAV-infected WT mice who received *Vim*$^{-/-}$ donor
379 bone marrow exhibited significantly lower total protein concentration in the BALF and lower
380 wet-to-dry lung weight ratio than mice that received WT donor bone marrow, indicating less
381 severe alveolar damage (**Figure 7b-c**). Mice showed no difference in IAV replication or
382 clearance regardless of donor genotype (**Figure 7d**). As in *Vim*$^{-/-}$ mice (**Figure 1**), WT mice
383 with *Vim*$^{-/-}$ MoAMs exhibited lower levels of pro-inflammatory cytokines and chemokines
384 (**Figure 7e**). Taken together, these data support the notion that vimentin-deficiency is
385 sufficient to alter MoAM function and provide protection to the host in response to IAV
386 infection. Thus, it follows that MoAMs that express a pro-inflammatory phenotype drive
387 lung injury following IAV infection.
388

389 **Discussion**

390 We used a clinically-relevant murine model of severe viral pneumonia to identify recruited
391 alveolar macrophage-specific gene expression patterns associated with three distinct
392 phases: Infiltrating, Early Inflammatory, and Late Inflammatory. WT MoAMs began
393 expressing pro-inflammatory genes and secreting tissue-damaging pro-inflammatory
394 cytokines in the Early Inflammatory phase, resulting in increased morbidity and mortality in

Figure 7

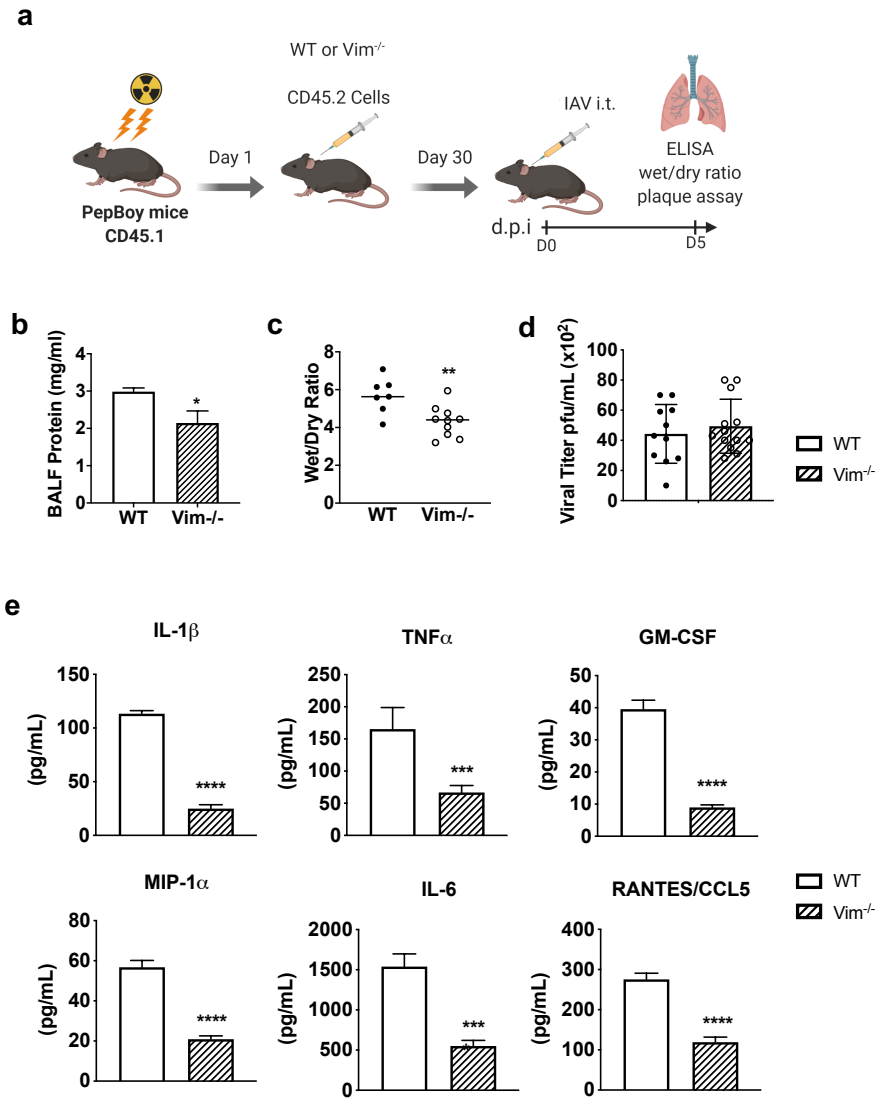

Figure 7. Vimentin-deficiency in the MoAM compartment is sufficient to protect from influenza A virus-induced lung damage and mortality. a) Schematic of the experimental design. Recipient mice (CD45.1) were irradiated and reconstituted with bone marrow cells from either WT or *Vim*$^{-/-}$ donor mice (CD45.2). After a 30-day recovery period, chimeric mice were intratracheally (i.t.) infected with a lethal dose of IAV at 5 days p.i. and subjected to analyses. **b)** Bronchoalveolar lavage fluid (BALF) protein levels measured by Bradford assay, n=3-4 **c)** Lung wet-to-dry ratio measured at day 5 p.i. n=7-10. **d**) Viral titer assessed by plaque assay. n=11-14. **e)** Levels of inflammatory cytokines in BALF assessed using a custom multiplex ELISA. n=4-9. Bar graphs represent mean, error bars represent SD. Differences between genotypes were assessed by t-test. * $p<0.05$, ** $p<0.001$, *** $p<0.0001$, **** $p<0.00001$.

Supplemental Figure 7

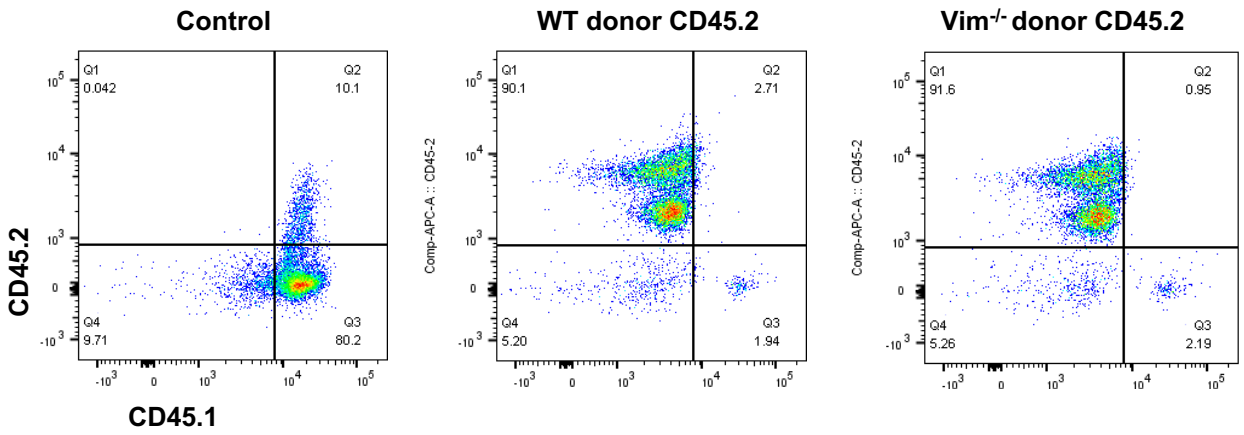

Supplemental Figure 7. Representative flow cytometry dot plots demonstrate successful engraftment of WT and *Vim*$^{-/-}$ CD45.2 donor cells into CD45.1 recipient mice.

395 influenza-infected wild-type mice. Conversely, *Vim*$^{-/-}$ mice suppressed the expression of
396 pro-inflammatory genes and the secretion of pro-inflammatory cytokines conferring
397 protection to the host. By leveraging *Vim*$^{-/-}$ mouse's protective phenotype, we identified a
398 core set of proinflammatory genes that drive lung injury and mortality. Although prior
399 studies have examined macrophage gene expression at steady-state or single time points
400 following IAV infection[4,42], by analyzing gene expression over a time course post-IAV
401 infection, our results identified critical temporal dynamics that shape the function of
402 recruited alveolar macrophages in response to respiratory infections.
403
404 *In vitro* studies have established vimentin's role in essential intracellular processes, such
405 as cell motility, cell signaling, protein complex scaffolding, and mechano-sensing through
406 the dynamic reorganization of vimentin intermediate filaments (IFs). In morphological
407 studies of circulating lymphocytes, lymphocyte extravasation was associated with the
408 pronounced reorganization of the vimentin IF network. Retinoic acid-inducible gene I, a
409 cytosolic PRR that detects viral RNA and mediates induction of type I interferon expression,
410 leads to increased vimentin expression[43]. Our data support this previous observation, as
411 type I interferon genes peaked on day 2 p.i., preceding the increase in vimentin gene
412 expression in WT MoAMs. We confirmed previous reports that *vimentin-deficient* mice fail
413 to secrete mature IL-1β, as assembly, and activation of the NLRP3 inflammasome requires
414 vimentin[17,18]. Complementary to our findings, vimentin's interaction with NOD2, a
415 cytoplasmic PRR, activated NF-κB and induced a proinflammatory immune response in an
416 inflammatory bowel disease model[16]. Collectively, these and our studies suggest that
417 vimentin mediates the innate immune response(s) through the dynamic reorganization of

418 its IF network, protein:protein interactions with PRRs, and regulating the expression of pro-
419 inflammatory genes. Our findings show that depleting vimentin in MoAMs modulates the
420 proinflammatory response and protects the host. It serves as a proof-of-principle to support
421 the development of pharmacological agents to target vimentin selectively. The tools may
422 be clinically beneficial in modulating the hyperinflammatory microenvironment of the virus-
423 infected lung.
424
425 We used a well-established bone-marrow chimera mouse model to demonstrate that *Vim*$^{-}$
426 $^{/-}$ MoAMs were sufficient to confer protection from IAV-induced lung injury and mortality.
427 However, by generating a *Vim*$^{fl/fl}$*Cx3cr1*^{CreERT2}*zsGreen* transgenic mouse, we could
428 selectively delete vimentin and track the recruitment of *GFP*$^{+}$*Vim*$^{-/-}$ alveolar macrophages
429 during IAV infection. Regrettably, the vimentin-floxed mouse is not yet available. Second,
430 our RNA-seq data identified distinct transcriptional phases of the IAV response in MoAMs;
431 however, it is unclear whether different MoAM subpopulations, as suggested by prior work[2],
432 entered the lung at different time points from a single compartment. For example, MoAMs
433 may differentiate directly from circulating monocytes that extravasate from the pulmonary
434 capillaries into the alveolar space. Alternatively, MoAMs may stem from interstitial
435 macrophages already residing in the lung at steady-state. Pulsed lineage tracing using the
436 *Vim*$^{fl/fl}$*Cx3cr1*^{CreERT2}*zsGreen* mouse would address these important questions.
437
438 In summary, we identified three distinct temporal patterns that characterize the
439 transcriptional response of MoAMs to IAV infection. Leveraging the protective phenotype
440 observed in *Vim*$^{-/-}$ mice, we identified a core set of pro-inflammatory genes whose

441 upregulation during the early response to IAV drives lung injury and mortality. We show
442 that vimentin-deficient MoAMs exhibit a dampened inflammatory response in a cell-
443 autonomous manner, sufficient to confer protection from IAV-induced mortality. Our
444 results define the temporal, transcriptional dynamics in recruited alveolar macrophages that
445 shape the response to respiratory infection and demonstrate that vimentin plays an
446 essential role in modifying macrophage phenotype and function.
447

448 **Materials & Methods**

449 ***In silico single cell RNA-seq data analysis.*** We queried a single cell RNA-seq
450 transcriptomic data set derived from bronchoalveolar lavage samples from 10 patients with
451 severe SARS-CoV-2 viral pneumonia[2]. We downloaded normalized counts tables and
452 visualized the pre-determined cell population clusters using Scanpy[44]. 40,000 single cells
453 representing the four monocyte-derived alveolar macrophages (MoAMs) populations were
454 visualized as an UMAP. Mean expression data of individual genes per cell population
455 cluster were visualized as dot plots in Scanpy.

456 ***Mice.*** All experiments were performed using wild-type or vimentin-null (*Vim*$^{-/-}$) 129S/V mice,
457 age 8-12 weeks. Wild-type mice were purchased from Taconic, *Vim*$^{-/-}$ mice were a gift from
458 Albee Messing (University of Wisconsin, Madison, WI). All animals were kept under
459 pathogen-free conditions, and all experiments were approved in accordance with
460 Northwestern University's Institutional Animal Care and Use Committee (IACUC)
461 guidelines.

462 ***Bone marrow chimeras***. 8-12 week old recipient mice (Ptprc^{a}/Pep-Boy, CD45.1) were
463 lethally irradiated with a single dose of 1,000 cGy γ-radiation using a Cs-137–based

464 Gammacell-40 irradiator (Nordion). Within 24 hours, fresh bone marrow cells (2 x 10^6) from
465 either WT donor mice or *Vim*$^{-/-}$ donor mice (CD45.2) were injected via retro-orbital injection.
466 Mice were housed together in individually ventilated cages and were given *ad libitum*
467 access to food and water supplemented with Trimetoprim/Sulfamethoxazole (TMP/SMX
468 40/8 mg formula, Hi-Tech Pharmacal) for 4 weeks and then switched to standard housing
469 regimen. Reconstituted mice were used for influenza infection experiments ~4 weeks after
470 transplantation. Engraftment was assessed after two weeks, using flow cytometry to
471 measure the percentage of CD45.1+ and CD45.2+ cells in peripheral blood collected from
472 the facial vein. All mice used for experiments showed reconstitution of the donor (CD45.2)
473 circulating leukocytes in peripheral blood above 85%.

474 ***Virus***. H1N1 Influenza virus strain A/WSN/1933 (WSN) was propagated in fertile chicken
475 eggs (Sunnyside Hatchery) as previously described[5,6]. Viral titers were determined by
476 measurement of plaque-forming units (pfu) in Madin-Darby canine kidney epithelial cells
477 (ATCC).

478 ***Plaque Assay.*** Confluent monolayers of Madin-Darby canine kidney epithelial cells were
479 infected with stock WSN virus in 1% BSA DMEM for 2h at 37°C. Plates were washed with
480 PBS and an overlay of 50% 2x replacement media (2x DMEM, 0.12M $NaHCO_3$, 2%
481 penicillin-streptomycin, and 1% HEPES), 50% Avicel (2.35%), and N-acetyl trypsin
482 (1.5μg/mL) remained on the cells for 72h at 37°C. Plates were washed with PBS and fixed
483 with 0.2% PFA before staining the monolayers with naphthalene blue-black stain.

484 ***In vivo influenza virus infection.*** 8-12 week old WT and *Vim*$^{-/-}$ 129S/V male mice were
485 anesthetized using isoflurane and intratracheally (i.t.) infected with 200 pfu WSN. Mice were
486 monitored daily, and weight was recorded every 24 hours.

487 ***Histology.*** Mice were euthanized, after which a 20-gauge angiocath was sutured into the
488 trachea. Heart and lungs were removed *en bloc*, and lungs were inflated with 0.8mL of 4%
489 paraformaldehyde (PFA) at a pressure not exceeding 16 cm H_2O. Tissue was fixed and
490 embedded in paraffin. 5 μm sections were stained with H&E by the Mouse Histology
491 Phenotyping Laboratory (Northwestern University, Chicago, IL). Tissue sections were
492 visualized using TissueGnostics, a Tissue/Cell High Throughput Imaging Analysis Systems
493 (Vienna, Austria) and captured using TissueFAXS software (TissueGnostics, Los Angeles,
494 CA) at the Northwestern University Cell Imaging Facility (Northwestern University, Chicago,
495 IL).
496 ***Bronchoalveolar Lavage.*** A 20-gauge angiocath was ligated into the trachea, and 1mL of
497 sterile PBS was instilled into the lungs, then removed through the angiocath. This process
498 was repeated three times. Bronchoalveolar lavage fluid (BALF) was centrifuged at 500 x *g*
499 for 10 min Protein levels in the supernatant were measured by Bradford assay (Bio-Rad),
500 and cytokine levels were measured using a custom multiplex ELISA (ThermoFisher
501 Scientific).
502 ***Wet-to-dry weight ratio.*** Mice were euthanized, and lungs were surgically removed *en*
503 *bloc*. The left lung was ligated, excised, and weighed in a tared container. The left lung was
504 dried at 70°C in a Speed-Vac SC100 evaporator (Thermo Scientific, Waltham, MA) until a
505 constant weight was obtained, and the wet-to-dry weight ratio was calculated.
506 ***Flow cytometry analysis of lung cell populations.*** Mice were euthanized, and lungs
507 were perfused with 10mL HBSS with Ca^{2+} and Mg^{2+}. Lung loves were removed and inflated
508 with enzyme solution (5mL of 0.2 mg/mL DNase I and 2 mg/mL collagenase D in HBSS
509 with Ca^{2+} and Mg^{2+}) using a 30-gauge needle. Tissue was minced and processed in

510 gentleMACS dissociator tubes according to the manufacturer's instructions (Miltenyi
511 Biotec). Processed lungs were passed through a 40μm cell strained, and RBCs were lysed
512 using BD PharmLyse (BD Biosciences, San Jose, CA). The remaining cells were counted
513 using a Countess cell counter (Invitrogen, Grand Island, NY). CD45 microbeads were
514 added, and cells were eluted according to the Miltenyi manufacturer's instructions. Cells
515 were stained with viability dye Aqua (Invitrogen), and non-specific antibody (Ab) binding
516 was inhibited by adding Fc Block (553142, clone 2.4G2; BD Pharmingen). Blocked cells
517 were stained with a mixture of fluorochrome-conjugated Abs (see **Online Supplemental**
518 **Table 1** for list of Abs). Data were acquired on a BD LSR II flow cytometer using BD
519 FACSDiva software (BD Biosciences), and data analyses were performed using FlowJo
520 software (Tree Star, Ashland, OR). Cell populations were identified using a sequential
521 gating strategy (**Supplemental Figure 1b)**. Cell number was normalized to body weight.
522 ***Macrophage harvesting and flow sort.*** Mice were euthanized and perfused with 5 mL
523 sterile PBS by cardiac perfusion through the right ventricle. A 20-gauge angiocath was
524 ligated into the trachea, and the lung and trachea were removed *en bloc*. Lungs were
525 instilled with 1 mL dispase (Corning) through the angiocath, and a second suture was tied
526 around the trachea to avoid leakage. Lungs were placed in 50 mL tubes (Falcon) containing
527 750 μL cold dispase and rocked for 45 min at RT. Trachea and angiocath were removed,
528 and lungs were minced using curved-edge scissors. Digested tissue was poured into 50
529 mL tubes containing 7 mL DMEM (Corning) and 14 μL DNase I (50 mg/mL, Sigma). Tubes
530 were rocked for 10 minutes at RT. Using serological pipettes, tissue was gently further
531 disrupted and subsequently filtered through 70 μm cell strainers and 40 μm strainers
532 (Corning). Tubes were rinsed with DMEM + 5% FBS and filtered through the same

533 strainers. Cell suspensions were centrifuged for 10 min at 1300 rpm, 4°C and pellets were
534 resuspended in 350 μL MACS buffer (Milteny). 100 μL CD11c magnetic microbeads
535 (Milteny) were added, and cells were eluted according to the Miltenyi manufacturer's
536 instructions. Cells were stained for CD11b (Biolegend), Siglec F (BD), Ly6C (eBioscience),
537 CD45 (eBioscience), MHCII (Biolegend), CD64 (Biolegend), Ly6G (BD), and NK1.1(BD).
538 Viability dye (eFluor506, eBioscience) was used to sort living cells only (**Online**
539 **Supplemental Table 1**). Using sequential gating (**Supplemental Figure 2b),** recruited
540 alveolar macrophages (MoAMs) and tissue-resident alveolar macrophages (TRAMs) were
541 flow-sorted using a BD FACSaria III 5-laser cell sorter and 100 μm nozzle (BD Biosciences).
542 Of note, MoAMs were collected in the same gate as interstitial macrophages (Ly6C-,
543 CD64+); however, by 2 days p.i., interstitial macrophages were no longer present in this
544 gate (see **Online Supplemental Figure 2**). Flow-sorted cells were collected into 1.5 mL
545 Eppendorf tubes containing 200 μL MACS buffer and centrifuged at 5,000 rpm for 5 min at
546 RT. Pellets were resuspended and lysed in RLT lysis buffer (Qiagen) and stored at -80°C
547 until all time points were collected.

548 ***RNA sequencing (RNA-seq).*** Samples collected from infected mice that at flow sort
549 appeared uninfected (had no infiltrating MoAM) were excluded from RNA isolation. RNA
550 was isolated in all samples at the same time to minimize the batch effect. All libraries for a
551 given cell type were prepared as a single batch for sequencing. Total RNA was isolated
552 using RNeasy Plus Mini kits (Qiagen). RNA quality (RIN) and quantity were assessed using
553 a TapeStation 4200 (Agilent Technologies). RIN scores ranged from 7.2 to 9.4, with an
554 average of 8.6. Using poly(A) mRNA magnetic enrichment kits from NEBNext (New
555 England Biolabs), mRNA was isolated. cDNA libraries were prepared using NEBNext Ultra

556 DNA library kits (New England BioLabs) for Illumina. Libraries were sequenced using high-
557 output 75-cycle single-end kits on an Illumina NextSeq 500 sequencer to an average depth
558 of 4.1 million reads per sample. Reads were demultiplexed (bcl2fastq), trimmed, and
559 aligned to reference genome mm10 using TopHat2[45]. Aligned reads were mapped to
560 genes using HTSeq with an Ensembl annotation (version 78)[46].
561 ***RNA-seq analysis.*** For k-means clustering, we used gene counts normalized to FPKM
562 (Fragments per Kilobase of transcript per Million mapped reads). Low counts were
563 removed, with a cut-off set as row sum >27 (# of samples used for analysis), yielding a
564 gene counts table of 9,169 expressed genes. One-way ANOVA with Benjamini-Hochberg
565 (BH) FDR correction was used to define differentially expressed genes over time. Genes
566 with an FDR <0.05 were considered differentially expressed, resulting in 2,623 DEGs.
567 Clustering was performed on the 2,623 DEGs using k-means clustering (GENE-E,
568 https://software.broadinstitute.org/GENE-E/index.html).
569 For pairwise comparison, low counts were trimmed if CPM <2 in all replicates in the smallest
570 group of the comparison. EdgeR was used to define pairwise differentially expressed genes
571 WT and Vim-/- MoAMs[47,48]. Principal Component analysis (PCA) plots were generated
572 using *pca* function in R. Pearson correlation matrix, and heatmaps were generated using
573 GENE-E. Gene ontology (GO) analysis was run using Gorilla[49,50]. Expressed genes, filtered
574 for low counts (9,169) were used as background. Gene set enrichment analysis (GSEA)
575 was run using the weighted pre-ranked setting based on the $\log_2$FC reported by edgeR
576 [51,52]. Gene sets associated with specific processes were downloaded from KEGG (Cell
577 Cycle) or Hallmark pathways (Glycolysis, Oxidative Phosphorylation, IFN alpha (Type I
578 interferon), IFNγ (Type II Interferon) with the exception of the custom gene sets described

579 below. The 85 overlapping genes between the IFNα and IFNγ Hallmark pathways were
580 excluded from the IFNγ gene set. Overlaps between gene lists were visualized using Venny
581 (https://bioinfogp.cnb.csic.es/tools/venny/index.html).
582 ***Custom gene set generation.*** Custom gene sets for LPS/IFNγ and IL-4 stimulated were
583 generated by querying primary published data available in relevant experimental models.
584 The final curated gene sets, $M_{(LPS/IFN\gamma)}$ and $M_{(IL\text{-}4)}$, were derived from four primary
585 publications[30-33]. All four publications used mouse bone-marrow-derived macrophages
586 (BMDM) and stimulated them *in vitro* with either LPS+IFNγor IL-4. Methodologies used
587 included LC-ESI-MS/MS mass spectrometry, microarray, and RNA-seq. A summary of the
588 experimental approach, methods, and results for all publications can be found in **Online**
589 **Supplemental Table 2**. We included all genes that were upregulated in at least one data
590 set and could be converted into a unique Ensembl ID. Three genes were found in both
591 $M_{(LPS/IFN\gamma)}$ and $M_{(IL\text{-}4)}$ and were removed to avoid any overlap between gene sets. These
592 trimming steps resulted in two annotated gene sets of 110 LPS/IFNγ stimulated genes and
593 101 IL-4 stimulated genes (**Online Supplemental Table 2**).
594 ***Motif finding.*** We generated two gene sets of the 186 most and 254 least changed genes
595 in *Vim*$^{-/-}$ MoAM by splitting the 440 genes of the Early Inflammatory cluster (Figure 2) based
596 on whether their $\log_2$(*Vim*$^{-/-}$/WT) expression on day 3 p.i. was above or below the mean of
597 -0.23. (**Figure 6d,e)**. To identify motifs that were enriched in either of these gene sets, we
598 ran findmotifs.pl from the HOMER package with default parameters and the mouse mm10
599 genome as background[39]. We identified significantly enriched motifs as those with p-value
600 < 0.05 in the known motif results.

601 ***Viral reads.*** To identify viral reads within libraries, unmapped reads were aligned to the
602 H1N1 reference genome. Reads for the H1N1 matrix protein 2 (M2), nucleoprotein (NP),
603 and neuraminidase (NA) were normalized by sample to the number of uniquely aligned
604 (mm10) reads.

605 ***Statistics.*** Analyses for cytokine levels, BALF protein, viral titer, and wet-to-dry ratio were
606 performed using GraphPad Prism (GraphPad Software). P values were calculated using a
607 two-tailed unpaired t-test assuming equal variance.

608

609 **Acknowledgments**

610 Histology services were provided by the Northwestern University Mouse Histology and
611 Phenotyping Laboratory, which is supported by NCI P30-CA060553 awarded to the Robert
612 H Lurie Comprehensive Cancer Center. Flow Cytometry was supported by the
613 Northwestern University RHLCCC Flow Cytometry Facility and a Cancer Center Support
614 Grant (NCI CA060553). This research was supported in part through the computational
615 resources and staff contributions provided by the Genomics Compute Cluster which is
616 jointly supported by the Feinberg School of Medicine, the Center for Genetic Medicine, and
617 Feinberg's Department of Biochemistry and Molecular Genetics, the Office of the Provost,
618 the Office for Research, and Northwestern Information Technology. The Genomics
619 Compute Cluster is part of Quest, Northwestern University's high performance computing
620 facility, with the purpose to advance research in genomics. Graphic design was created
621 with BioRender.com. Kishore R. Anekalla was supported by NIH T32 HL076139. Shang-
622 Yang Chen was supported by a pre-doctoral AHA award (19PRE34380200). Alexander V.
623 Misharin was supported by N.I.H. grants U19AI135964, P01AG049665, R01HL153312,

and NUCATS COVID-19 Rapid Response Grant. Karen M. Ridge was supported by N.I.H. grants P01AG049665 and P01GM096971. Bria M. Coates was supported by funds provided by the Manne Research Institute COVID-19 Springboard Exploratory Research Award and N.I.H. grant K08HL143127. Deborah R. Winter `was supported by the American Lung Association, Arthritis National Research Foundation, American Thoracic Society, Scleroderma Foundation, American Federation for Aging Research, American Heart Association 18CDA34110224, and NIH/NIAID U19AI135964. G.R.S.B. was supported by NIH grants U19AI135964, P01AG049665, P01AG04966506S1, R01HL147575 and Veterans Affairs grant I01CX001777.

Author contributions: C.M.K., K.R.A., Y.H., B.M.C., A.V.M., D.R.W., K.M.R., contributed to the acquisition, analysis, and interpretation of the data and drafting the manuscript. M.C., G.G., S.C., M.T., Y.C., J.M.D., contributed to the acquisition and interpretation of data. C.M.K., K.R.A., Y.H., B.M.C., H.A.V., P.A.R., A.V.M., G.R.S.B., D.R.W., K.M.R. contributed to the conception and design of the study and interpretation of the data. All authors critically revised and approved the final version of the manuscript.

642 **References**
643

644 1. Jain, S., Self, W.H., Wunderink, R.G., Fakhran, S., Balk, R., Bramley, A.M., Reed, C., Grijalva,
645 C.G., Anderson, E.J., Courtney, D.M., Chappell, J.D., Qi, C., Hart, E.M., Carroll, F., Trabue,
646 C., Donnelly, H.K., Williams, D.J., Zhu, Y., Arnold, S.R., Ampofo, K., Waterer, G.W., Levine,
647 M., Lindstrom, S., Winchell, J.M., Katz, J.M., Erdman, D., Schneider, E., Hicks, L.A., McCullers,
648 J.A., Pavia, A.T., Edwards, K.M., Finelli, L. & Team, C.E.S. Community-acquired pneumonia
649 requiring hospitalization among u.S. Adults. *N Engl J Med* 373, 415-427 (2015) PMC4728150.
650 2. Grant, R.A., Morales-Nebreda, L., Markov, N.S., Swaminathan, S., Querrey, M., Guzman, E.R.,
651 Abbott, D.A., Donnelly, H.K., Donayre, A., Goldberg, I.A., Klug, Z.M., Borkowski, N., Lu, Z.,
652 Kihshen, H., Politanska, Y., Sichizya, L., Kang, M., Shilatifard, A., Qi, C., Lomasney, J.W.,
653 Argento, A.C., Kruser, J.M., Malsin, E.S., Pickens, C.O., Smith, S.B., Walter, J.M., Pawlowski,
654 A.E., Schneider, D., Nannapaneni, P., Abdala-Valencia, H., Bharat, A., Gottardi, C.J.,
655 Budinger, G.R.S., Misharin, A.V., Singer, B.D. & Wunderink, R.G. Circuits between infected
656 macrophages and t cells in sars-cov-2 pneumonia. *Nature* (2021)
657 3. Calfee, C.S., Delucchi, K., Parsons, P.E., Thompson, B.T., Ware, L.B. & Matthay, M.A.
658 Subphenotypes in acute respiratory distress syndrome: Latent class analysis of data from two
659 randomised controlled trials. *Lancet Respir Med* 2, 611-620 (2014) PMC4154544.
660 4. Tate, M.D., Pickett, D.L., van Rooijen, N., Brooks, A.G. & Reading, P.C. Critical role of airway
661 macrophages in modulating disease severity during influenza virus infection of mice. *Journal*
662 *of Virology* 84, 7569-7580 (2010)
663 5. Coates, B.M., Staricha, K.L., Koch, C.M., Cheng, Y., Shumaker, D.K., Budinger, G.R.S.,
664 Perlman, H., Misharin, A.V. & Ridge, K.M. Inflammatory monocytes drive influenza a virus-
665 mediated lung injury in juvenile mice. *J Immunol* 200, 2391-2404 (2018) PMC5860989.
666 6. Misharin, A.V., Morales-Nebreda, L., Reyfman, P.A., Cuda, C.M., Walter, J.M., McQuattie-
667 Pimentel, A.C., Chen, C.I., Anekalla, K.R., Joshi, N., Williams, K.J.N., Abdala-Valencia, H.,
668 Yacoub, T.J., Chi, M., Chiu, S., Gonzalez-Gonzalez, F.J., Gates, K., Lam, A.P., Nicholson,
669 T.T., Homan, P.J., Soberanes, S., Dominguez, S., Morgan, V.K., Saber, R., Shaffer, A.,
670 Hinchcliff, M., Marshall, S.A., Bharat, A., Berdnikovs, S., Bhorade, S.M., Bartom, E.T.,
671 Morimoto, R.I., Balch, W.E., Sznajder, J.I., Chandel, N.S., Mutlu, G.M., Jain, M., Gottardi, C.J.,
672 Singer, B.D., Ridge, K.M., Bagheri, N., Shilatifard, A., Budinger, G.R.S. & Perlman, H.
673 Monocyte-derived alveolar macrophages drive lung fibrosis and persist in the lung over the life
674 span. *J Exp Med* 214, 2387-2404 (2017) PMC5551573.
675 7. Yona, S., Kim, K.-W., Wolf, Y., Mildner, A., Varol, D., Breker, M., Strauss-Ayali, D., Viukov, S.,
676 Guilliams, M., Misharin, A., Hume, David A., Perlman, H., Malissen, B., Zelzer, E. & Jung, S.
677 Fate mapping reveals origins and dynamics of monocytes and tissue macrophages under
678 homeostasis. *Immunity* 38, 79-91 (2013)
679 8. Allen, I.C., Scull, M.A., Moore, C.B., Holl, E.K., McElvania-TeKippe, E., Taxman, D.J., Guthrie,
680 E.H., Pickles, R.J. & Ting, J.P. The nlrp3 inflammasome mediates in vivo innate immunity to
681 influenza a virus through recognition of viral rna. *Immunity* 30, 556-565 (2009) PMC2803103.
682 9. Thomas, P.G., Dash, P., Aldridge, J.R., Jr., Ellebedy, A.H., Reynolds, C., Funk, A.J., Martin,
683 W.J., Lamkanfi, M., Webby, R.J., Boyd, K.L., Doherty, P.C. & Kanneganti, T.D. The intracellular
684 sensor nlrp3 mediates key innate and healing responses to influenza a virus via the regulation
685 of caspase-1. *Immunity* 30, 566-575 (2009) PMC2765464.
686 10. Coates, B.M., Staricha, K.L., Ravindran, N., Koch, C.M., Cheng, Y., Davis, J.M., Shumaker,
687 D.K. & Ridge, K.M. Inhibition of the nod-like receptor protein 3 inflammasome is protective in
688 juvenile influenza a virus infection. *Front Immunol* 8, 782 (2017) PMC5502347.
689 11. Tate, M.D., Ong, J.D., Dowling, J.K., McAuley, J.L., Robertson, A.B., Latz, E., Drummond,
690 G.R., Cooper, M.A., Hertzog, P.J. & Mansell, A. Reassessing the role of the nlrp3
691 inflammasome during pathogenic influenza a virus infection via temporal inhibition. *Sci Rep* 6,
692 27912 (2016) PMC4901306.

12. Dawson, T.C., Beck, M.A., Kuziel, W.A., Henderson, F. & Maeda, N. Contrasting effects of ccr5 and ccr2 deficiency in the pulmonary inflammatory response to influenza a virus. *Am J Pathol* 156, 1951-1959 (2000) PMC1850091.
13. Lin, K.L., Sweeney, S., Kang, B.D., Ramsburg, E. & Gunn, M.D. Ccr2-antagonist prophylaxis reduces pulmonary immune pathology and markedly improves survival during influenza infection. *J Immunol* 186, 508-515 (2011) PMC3723340.
14. Mor-Vaknin, N., Legendre, M., Yu, Y., Serezani, C.H., Garg, S.K., Jatzek, A., Swanson, M.D., Gonzalez-Hernandez, M.J., Teitz-Tennenbaum, S., Punturieri, A., Engleberg, N.C., Banerjee, R., Peters-Golden, M., Kao, J.Y. & Markovitz, D.M. Murine colitis is mediated by vimentin. *Sci Rep* 3, 1045 (2013) PMC3540396.
15. Kamphuis, W., Kooijman, L., Orre, M., Stassen, O., Pekny, M. & Hol, E.M. Gfap and vimentin deficiency alters gene expression in astrocytes and microglia in wild-type mice and changes the transcriptional response of reactive glia in mouse model for alzheimer's disease. *Glia* 63, 1036-1056 (2015)
16. Stevens, C., Henderson, P., Nimmo, E.R., Soares, D.C., Dogan, B., Simpson, K.W., Barrett, J.C., International Inflammatory Bowel Disease Genetics, C., Wilson, D.C. & Satsangi, J. The intermediate filament protein, vimentin, is a regulator of nod2 activity. *Gut* 62, 695-707 (2013) PMC4225453.
17. dos Santos, G., Rogel, M.R., Baker, M.A., Troken, J.R., Urich, D., Morales-Nebreda, L., Sennello, J.A., Kutuzov, M.A., Sitikov, A., Davis, J.M., Lam, A.P., Cheresh, P., Kamp, D., Shumaker, D.K., Budinger, G.R. & Ridge, K.M. Vimentin regulates activation of the nlrp3 inflammasome. *Nat Commun* 6, 6574 (2015) PMC4358756.
18. Lang, T., Lee, J.P.W., Elgass, K., Pinar, A.A., Tate, M.D., Aitken, E.H., Fan, H., Creed, S.J., Deen, N.S., Traore, D.A.K., Mueller, I., Stanisic, D., Baiwog, F.S., Skene, C., Wilce, M.C.J., Mansell, A., Morand, E.F. & Harris, J. Macrophage migration inhibitory factor is required for nlrp3 inflammasome activation. *Nat Commun* 9, 2223 (2018) PMC5993818.
19. Cai, B., Kasikara, C., Doran, A.C., Ramakrishnan, R., Birge, R.B. & Tabas, I. Mertk signaling in macrophages promotes the synthesis of inflammation resolution mediators by suppressing camkii activity. *Sci Signal* 11 (2018) PMC6171110.
20. Xu-Vanpala, S., Deerhake, M.E., Wheaton, J.D., Parker, M.E., Juvvadi, P.R., MacIver, N., Ciofani, M. & Shinohara, M.L. Functional heterogeneity of alveolar macrophage population based on expression of cxcl2. *Sci Immunol* 5 (2020) PMC7717592.
21. Imai, T., Hieshima, K., Haskell, C., Baba, M., Nagira, M., Nishimura, M., Kakizaki, M., Takagi, S., Nomiyama, H., Schall, T.J. & Yoshie, O. Identification and molecular characterization of fractalkine receptor cx3cr1, which mediates both leukocyte migration and adhesion. *Cell* 91, 521-530 (1997)
22. Worthylake, R.A. & Burridge, K. Rhoa and rock promote migration by limiting membrane protrusions. *J Biol Chem* 278, 13578-13584 (2003)
23. Lämmermann, T., Bader, B.L., Monkley, S.J., Worbs, T., Wedlich-Söldner, R., Hirsch, K., Keller, M., Förster, R., Critchley, D.R., Fässler, R. & Sixt, M. Rapid leukocyte migration by integrin-independent flowing and squeezing. *Nature* 453, 51-55 (2008)
24. Starnes, T., Rasila, K.K., Robertson, M.J., Brahmi, Z., Dahl, R., Christopherson, K. & Hromas, R. The chemokine cxcl14 (brak) stimulates activated nk cell migration: Implications for the downregulation of cxcl14 in malignancy. *Exp Hematol* 34, 1101-1105 (2006)
25. Herold, S., Becker, C., Ridge, K.M. & Budinger, G.R. Influenza virus-induced lung injury: Pathogenesis and implications for treatment. *Eur Respir J* 45, 1463-1478 (2015)
26. Kratofil, R.M., Kubes, P. & Deniset, J.F. Monocyte conversion during inflammation and injury. *Arterioscler Thromb Vasc Biol* 37, 35-42 (2017)
27. Sanchez, K.K., Chen, G.Y., Schieber, A.M.P., Redford, S.E., Shokhirev, M.N., Leblanc, M., Lee, Y.M. & Ayres, J.S. Cooperative metabolic adaptations in the host can favor asymptomatic infection and select for attenuated virulence in an enteric pathogen. 175, 146-158.e115 (2018)

744 28. Smallwood, H.S., Duan, S., Morfouace, M., Rezinciuc, S., Shulkin, B.L., Shelat, A., Zink, E.E.,
745 Milasta, S., Bajracharya, R., Oluwaseum, A.J., Roussel, M.F., Green, D.R., Pasa-Tolic, L. &
746 Thomas, P.G. Targeting metabolic reprogramming by influenza infection for therapeutic
747 intervention. *Cell Reports* 19, 1640-1653 (2017)
748 29. Singer, B.D. & Chandel, N.S. Immunometabolism of pro-repair cells. 129, 2597-2607 (2019)
749 30. Jablonski, K.A., Amici, S.A., Webb, L.M., Ruiz-Rosado Jde, D., Popovich, P.G., Partida-
750 Sanchez, S. & Guerau-de-Arellano, M. Novel markers to delineate murine m1 and m2
751 macrophages. *PLoS One* 10, e0145342 (2015) PMC4689374.
752 31. Hans, C.P., Sharma, N., Sen, S., Zeng, S., Dev, R., Jiang, Y., Mahajan, A. & Joshi, T.
753 Transcriptomics analysis reveals new insights into the roles of notch1 signaling on macrophage
754 polarization. 9, 7999 (2019)
755 32. Gensel, J.C., Kopper, T.J., Zhang, B., Orr, M.B. & Bailey, W.M. Predictive screening of m1 and
756 m2 macrophages reveals the immunomodulatory effectiveness of post spinal cord injury
757 azithromycin treatment. *Sci Rep* 7, 40144 (2017) PMC5216345.
758 33. Becker, L., Liu, N.C., Averill, M.M., Yuan, W., Pamir, N., Peng, Y., Irwin, A.D., Fu, X., Bornfeldt,
759 K.E. & Heinecke, J.W. Unique proteomic signatures distinguish macrophages and dendritic
760 cells. *PLoS ONE [Electronic Resource]* 7, e33297 (2012)
761 34. Misharin, A.V., Morales-Nebreda, L., Mutlu, G.M., Budinger, G.R. & Perlman, H. Flow
762 cytometric analysis of macrophages and dendritic cell subsets in the mouse lung. *Am J Respir*
763 *Cell Mol Biol* 49, 503-510 (2013) PMC3824047.
764 35. Landsman, L. & Jung, S. Lung macrophages serve as obligatory intermediate between blood
765 monocytes and alveolar macrophages. *J Immunol* 179, 3488-3494 (2007)
766 36. Gosselin, D., Link, V.M., Romanoski, C.E., Fonseca, G.J., Eichenfield, D.Z., Spann, N.J.,
767 Stender, J.D., Chun, H.B., Garner, H., Geissmann, F. & Glass, C.K. Environment drives
768 selection and function of enhancers controlling tissue-specific macrophage identities. *Cell* 159,
769 1327-1340 (2014) PMC4364385.
770 37. Ostuni, R., Piccolo, V., Barozzi, I., Polletti, S., Termanini, A., Bonifacio, S., Curina, A.,
771 Prosperini, E., Ghisletti, S. & Natoli, G. Latent enhancers activated by stimulation in
772 differentiated cells. *Cell* 152, 157-171 (2013)
773 38. Lavin, Y., Winter, D., Blecher-Gonen, R., David, E., Keren-Shaul, H., Merad, M., Jung, S. &
774 Amit, I. Tissue-resident macrophage enhancer landscapes are shaped by the local
775 microenvironment. *Cell* 159, 1312-1326 (2014) PMC4437213.
776 39. Heinz, S., Benner, C., Spann, N., Bertolino, E., Lin, Y.C., Laslo, P., Cheng, J.X., Murre, C.,
777 Singh, H. & Glass, C.K. Simple combinations of lineage-determining transcription factors prime
778 cis-regulatory elements required for macrophage and b cell identities. *Mol Cell* 38, 576-589
779 (2010) PMC2898526.
780 40. Heinz, S., Romanoski, C.E., Benner, C., Allison, K.A., Kaikkonen, M.U., Orozco, L.D. & Glass,
781 C.K. Effect of natural genetic variation on enhancer selection and function. *Nature* 503, 487-
782 492 (2013) PMC3994126.
783 41. Seifert, L.L., Si, C., Saha, D., Sadic, M., de Vries, M., Ballentine, S., Briley, A., Wang, G.,
784 Valero-Jimenez, A.M., Mohamed, A., Schaefer, U., Moulton, H.M., García-Sastre, A., Tripathi,
785 S., Rosenberg, B.R. & Dittmann, M. The ets transcription factor elf1 regulates a broadly
786 antiviral program distinct from the type i interferon response. *PLoS Pathog* 15, e1007634
787 (2019) PMC6932815.
788 42. Zhang, J., Liu, J., Yuan, Y., Huang, F., Ma, R., Luo, B., Xi, Z., Pan, T., Liu, B., Zhang, Y.,
789 Zhang, X., Luo, Y., Wang, J., Zhao, M., Lu, G., Deng, K. & Zhang, H. Two waves of pro-
790 inflammatory factors are released during the influenza a virus (iav)-driven pulmonary
791 immunopathogenesis. 16, e1008334 (2020)
792 43. de Rivero Vaccari, J.P., Minkiewicz, J., Wang, X., De Rivero Vaccari, J.C., German, R.,
793 Marcillo, A.E., Dietrich, W.D. & Keane, R.W. Astrogliosis involves activation of retinoic acid-

794 inducible gene-like signaling in the innate immune response after spinal cord injury. *Glia* 60,
795 414-421 (2012) PMC3265608.
796 44. Wolf, F.A., Angerer, P. & Theis, F.J. Scanpy: Large-scale single-cell gene expression data
797 analysis. *Genome Biol* 19, 15 (2018) PMC5802054.
798 45. Kim, D., Pertea, G., Trapnell, C., Pimentel, H., Kelley, R. & Salzberg, S.L. Tophat2: Accurate
799 alignment of transcriptomes in the presence of insertions, deletions and gene fusions. 14, R36
800 (2013)
801 46. Anders, S., Pyl, P.T. & Huber, W. Htseq--a python framework to work with high-throughput
802 sequencing data. *Bioinformatics* 31, 166-169 (2015) PMC4287950.
803 47. Robinson, M.D., McCarthy, D.J. & Smyth, G.K. Edger: A bioconductor package for differential
804 expression analysis of digital gene expression data. *Bioinformatics* 26, 139-140 (2010)
805 PMC2796818.
806 48. McCarthy, D.J., Chen, Y. & Smyth, G.K. Differential expression analysis of multifactor rna-seq
807 experiments with respect to biological variation. *Nucleic Acids Res* 40, 4288-4297 (2012)
808 PMC3378882.
809 49. Eden, E., Lipson, D., Yogev, S. & Yakhini, Z. Discovering motifs in ranked lists of DNA
810 sequences. *PLoS Comput Biol* 3, e39 (2007) PMC1829477.
811 50. Eden, E., Navon, R., Steinfeld, I., Lipson, D. & Yakhini, Z. Gorilla: A tool for discovery and
812 visualization of enriched go terms in ranked gene lists. *BMC Bioinformatics* 10, 48 (2009)
813 PMC2644678.
814 51. Mootha, V.K., Lindgren, C.M., Eriksson, K.F., Subramanian, A., Sihag, S., Lehar, J.,
815 Puigserver, P., Carlsson, E., Ridderstr*ale, M., Laurila, E., Houstis, N., Daly, M.J., Patterson,
816 N., Mesirov, J.P., Golub, T.R., Tamayo, P., Spiegelman, B., Lander, E.S., Hirschhorn, J.N.,
817 Altshuler, D. & Groop, L.C. Pgc-1alpha-responsive genes involved in oxidative phosphorylation
818 are coordinately downregulated in human diabetes. 34, 267-273 (2003)
819 52. Subramanian, A., Tamayo, P., Mootha, V.K., Mukherjee, S., Ebert, B.L., Gillette, M.A.,
820 Paulovich, A., Pomeroy, S.L., Golub, T.R., Lander, E.S. & Mesirov, J.P. Gene set enrichment
821 analysis: A knowledge-based approach for interpreting genome-wide expression profiles. *Proc*
822 *Natl Acad Sci U S A* 102, 15545-15550 (2005) PMC1239896.

823
824

825 **Figure Legends**
826
827 **Figure 1. Vimentin-null mice are protected from influenza-induced lung injury and**
828 **mortality. a**) Uniform Manifold Approximation and Projection (UMAP) of 40,248 cells
829 annotated as monocyte-derived alveolar macrophages (MoAMs) obtained from 10 patients
830 with severe COVID-19 disease within 48 hours after intubation. **b)** Fraction of cells
831 expressing *VIM* and mean expression in each MoAM cluster. **c)** Visualization of *IL1-B,*
832 *CCL3, CXCL2, C1QA*, and *MERTK* expression in MoAM cells using density projection
833 plots. Scale bar represents expression averaged within hexagonal areas on UMAP. **d)**
834 Fraction of cells expressing the representative genes and their mean expression in each
835 MoAM cluster . **e)** Survival of wild-type (WT) and *Vim*$^{-/-}$ mice intratracheally infected with a
836 lethal dose of influenza A virus (IAV) (200pfu) was measured and compared. Survival
837 curves were analyzed using log-rank test, p-value =0.001. Data shown are n=12 per group.
838 **f**) Lung wet-to-dry ratio measured at day 3 and 5 p.i. (n = 8-11/timepoint) **g**) Bronchoalveolar
839 lavage fluid (BALF) protein levels measured by Bradford assay, n=5/timepoint. In **f** and **g**,
840 differences between genotypes on each day were assessed by t-test. p-values were 0.0015
841 and <0.0001, for 3 and 5 days p.i., respectively. **h)** Representative images of murine lung
842 architecture assessed by H&E staining, scale bar 100 um. **i**) Viral titer assessed by plaque
843 assay. Difference between genotypes was statistically not significant. n=5-9/timepoint. **j**)
844 Flow cytometric analysis of tissue resident (TRAMs) and infiltrating monocyte-derived
845 alveolar macrophages (MoAMs) out of the total lung CD45+ cell population normalized to
846 body weight during the IAV response, n=4/timepoint. **k)** Levels of inflammatory cytokines
847 in BALF were assessed using a custom multiplex ELISA. n=3-4/timepoint. Bar graphs
848 represent mean, error bars represent SD, differences between genotypes on each day
849 were assessed by t-test. * p<0.05, ** p<0.001, *** p<0.0001, **** p<0.00001.
850
851
852 **Supplemental Figure 1**. **a**) UMAP of 77,146 cells annotated by cell type obtained from 10
853 patients with severe COVID-19 disease within 48 hours after intubation. **b)** Fraction of cells
854 expressing the representative genes and their mean expression in each TRAM cluster. **c)**
855 Quantification of H1N1 viral RNA molecules detected among RNA isolated from MoAMs,
856 normalized to the number of reads uniquely aligned to mouse genome (mm10) for each
857 sample. Bar graphs represent mean, error bars represent SD. **d)** Gating strategy used for
858 flow cytometry analysis of neutrophils, TRAMs, interstitial macrophages (IM) and MoAMs.
859 **e**) Flow cytometric analysis demonstrated no differences in number of neutrophils out of
860 the total lung CD45+ cell population normalized to body weight between *Vim*$^{-/-}$ and WT
861 mice during the IAV response.
862
863 **Figure 2. Wild-type monocyte-derived alveolar macrophages exhibit gene**
864 **expression patterns associated with three phases of influenza A viral infection. a)**
865 Heatmap of normalized expression of 2,623 differentially expressed genes (ANOVA
866 adjusted p-value <0.05). Z-score normalization for each row was applied to gene
867 expression (FPKM) data. K-means clustering (k=3) identified three clusters; Infiltrating
868 (1131 genes), Early Inflammatory (440 genes), Late Inflammatory (1052 genes). **b)** Mean
869 z-scores calculated across genes for each cluster **c)** Gene Ontology (GO) term enrichment
870 for each phase. **d)** Bar graphs of gene expression (FPKM) for representative genes in each

phase. Error bars represent SD. (ANOVA adjusted p-value <0.05). **e)** Bubble plot representing the proportion of genes (%) within each process that had an expression above the row mean. Color gradient represents mean z-score of expression across genes. **f)** Enrichment of gene sets in each cluster as defined in A. Asterisk represents significantly enriched overlaps (hypergeometric p-value <0.0018, FWER = 0.05). Dotted line indicates expected enrichment score of 1. n=3-4 per group. Ox Phos = Oxidative phosphorylation.

Supplemental Figure 2. a) Schematic of experimental design and workflow. WT or *Vim*$^{-/-}$ mice were infected with a lethal dose of influenza A virus (200 pfu). MoAMs were sorted by flow cytometry (FACS) from lungs on 2, 3, 4, and 6 days p.i. Total RNA was isolated, mRNA was enriched, and bulk RNA-seq was performed. Principal component analysis (PCA) was used to visualize replicates. **b)** Sequential gating strategy used for FACS collection of TRAMs and MoAMs **c)** Violin plots of $\log_2$(FPKM+1) counts data for all genes in each cluster. Solid lines represent median, dotted lines represent quartiles. **d)** Bar graphs of gene expression (FPKM) in MoAM for representative genes in each phase. Error bars represent SD. (ANOVA adjusted p-value <0.05).

Figure 3. Wild-type monocyte-derived alveolar macrophages resemble interstitial macrophages during the infiltrating phase and exhibit increased expression of alveolar macrophages genes over time. a) Volcano plot of differentially expressed genes (edgeR p-value<0.05, and edgeR reported log2FC>|1.0|) between TRAM and IM at steady-state (0 dpi). The number of genes increased (red) and decreased (blue) in TRAMs compared to IMs are shown. **b)** Mean z-scores calculated for IM- and TRAM-specific gene sets over the course of IAV infection in MoAMs **c)** Plots representing % of genes at each time point expressed above the mean. Each dot represents a replicate. Lines represent median. **d)** Bar graphs of gene expression (FPKM) for representative genes in IM- and TRAM-specific gene sets. Error bars represent SD. **e)** Enrichment of IM- and TRAM-cell specific gene signatures in MoAMs for each phase. Asterisk represents significantly enriched overlaps (hypergeometric p-value <0.006, FWER = 0.05).

Figure 4. *Vim-/-* MoAMs exhibit increased expression of Infiltrating phase genes and decreased expression of Early Inflammatory phase genes. a) Heatmap of normalized expression of 2,623 genes as defined in Figure 2a. *Vim*$^{-/-}$ data was normalized to the WT mean and standard deviation (adapted z-score). **b**) Mean adapted z-scores were calculated across genes for each cluster in WT MoAMs and *Vim*$^{-/-}$ MoAMs. Shading represents WT MoAMs inter-quartile range (IQR) **c**) Bar graphs representing the fold change in gene expression (FPKM) in *Vim*$^{-/-}$ MoAMs compared to the WT MoAMs mean for representative genes. (n=3-4 per group). **d)** % genes in each cluster that exhibit decreased or increased expression in *Vim*$^{-/-}$ MoAMs compared to WT MoAMs (n=3-4 per group). Decreased genes defined as $\log_2$FC < -0.58 (FC of 1.5); increased genes defined as $\log_2$FC>0.58.

Supplemental Figure 4. a) Principal component analysis (PCA) of *Vim*$^{-/-}$ MoAMs replicates. **b)** Violin plots representing the $\log_2$FC between *Vim*$^{-/-}$ and WT for each gene by cluster in MoAMs. Solid lines represent median, dotted lines represent quartiles. **c)** Heatmap showing pairwise Pearson correlation of mean gene expression across replicates between each time point in WT and *Vim*$^{-/-}$ MoAMs. Pearson correlation coefficient values

917 shown within each square. Scale bar represents Pearson correlation coefficient. **d)** Violin
918 plots representing the log_2FC between days p.i. for each gene by cluster in WT and *Vim*$^{-/-}$
919 MoAMs. Solid lines represent median, dotted lines represent quartiles. **e)** Violin plots
920 representing the log_2FC between *Vim*$^{-/-}$ and WT in TRAMs and IMs at steady-state (0 dpi)
921 for each gene by cluster. Solid lines represent median, dotted lines represent quartiles. **f)**
922 Heatmap of normalized expression of 2,623 differentially expressed genes in *Vim*$^{-/-}$ MoAMs
923 (ANOVA adjusted p-value <0.05). Adapted Z-score normalization for each row was applied
924 to gene expression (FPKM) data using *Vim*$^{-/-}$ MoAMs mean and standard deviation. K-
925 means clustering (k=3) was performed on *Vim*$^{-/-}$ MoAMs expression and WT MoAMs data
926 was visualized for the same genes **g**) Mean adapted z-scores were calculated across
927 genes for each cluster in *Vim*$^{-/-}$ and WT MoAMs. Shading represents *Vim*$^{-/-}$ MoAMs IQR.
928
929 **Figure 5. Inflammatory pathways are consistently decreased in *Vim*$^{-/-}$ MoAMs**
930 **compared to WT MoAMs during influenza A infection. a)** Volcano plots of differentially
931 expressed genes (edgeR p-value<0.05, and edgeR reported $log_2FC>|1.0|$) between *Vim*$^{-/-}$
932 and WT MoAMs on each day post-infection. The number of genes increased (red) and
933 decreased (blue) in *Vim*$^{-/-}$ compared to WT MoAMs are shown. **b)** GO term enrichment
934 across days p.i. in the increased (red) and decreased (blue) genes in *Vim*$^{-/-}$ compared to
935 WT MoAMs. Scale represents $-log_{10}$ p-value. **c)** Violin plots representing the log_2FC for
936 each process between *Vim*$^{-/-}$ and WT MoAMs. Solid lines represent median, dotted lines
937 represent quartiles. **d)** Scatter plots of z-score normalized gene expression across genes
938 in $M_{(IL-4)}$ vs Cell Cycle. Pearson correlation coefficients (r) across WT or *Vim*$^{-/-}$ MoAM
939 replicates and associated p-values are shown. **e)** Heatmap matrix of Pearson correlation
940 between processes, asterisk indicate p-value <0.05.
941
942 **Supplemental Figure 5. a)** Plots representing % of genes at each time point expressed
943 above their WT mean. Each dot represents a replicate. Lines represent median. **b, c)** Gene
944 Set Enrichment Analysis (GSEA) enrichment plots. GSEA was performed on gene lists
945 ranked by edgeR reported fold-change between *Vim*$^{-/-}$ and WT MoAMs at each time point.
946 Normalized enrichment scores (NES) are shown. Asterisks indicate statistically significant
947 adjusted p-values <0.05. **d)** Violin plots representing the log_2FC between *Vim*$^{-/-}$ and WT
948 TRAMs and IMs at steady-state (0 dpi). Solid lines represent medians, dashed lines
949 represent quartiles.
950
951 **Figure 6. Protective phenotype of *Vim*$^{-/-}$mice is associated with the failure of *Vim*$^{-/-}$**
952 **MoAMs to activate core pro-inflammatory genes in the early response to IAV. a)** Percent
953 (%) $M_{(LPS)}$ genes peaking in expression on each day post-infection in WT and *Vim*$^{-/-}$ MoAMs
954 **b)** Bar graphs of gene expression (FPKM) for representative $M_{(LPS)}$ genes present in the
955 leading edge of at least 1 day from GSEA. Error bars represent SD. **c)** Heatmap of
956 normalized expression of 84 $M_{(LPS)}$ genes present in the GSEA leading edge on at least 1
957 day (indicated by color-coded bar on left). Adapted Z-score normalization using WT mean
958 and standard deviation for each row was applied to gene expression (FPKM) data. **d)**
959 Histogram representing the distribution of log_2FC between *Vim*$^{-/-}$ and WT MoAMs on 3 dpi
960 of the Early Inflammatory phase (440 genes). Dashed line represents mean of the
961 distribution. Number of genes less than (186) and greater than (254) the mean are shown.
962 Genes with log_2FC between *Vim*$^{-/-}$ and WT MoAMs less than the mean represent those

963 genes that are most changed between *Vim*$^{-/-}$ and WT MoAMs. **e)** Mean adapted z-scores
964 were calculated across genes for most (186) and least (254) changed genes on 3 dpi in the
965 Early Inflammatory Phase in WT and *Vim*$^{-/-}$ MoAMs. **f)** HOMER known motif analysis using
966 genomic background of most changed genes on 3 dpi in the Early Inflammatory Phase (186
967 genes). Motif logos are shown below motif names. -$\log_{10}$pvalues of enrichment in most or
968 least changed gene set is shown. Log_2(FPKM+1) average gene expression of transcription
969 factor family members are shown for WT TRAMs and WT IMs at steady-state (0 dpi) and
970 2-6 dpi for WT MoAMs. $\log_2$FC between *Vim*$^{-/-}$ and WT MoAM gene expression of
971 transcription factor family members on each dpi. (n=3-4)
972
973 **Supplemental Figure 6. a)** Mean adapted z-scores for $M_{(LPS)}$ and $M_{(IL\text{-}4)}$ genes present in
974 the leading edge of at least 1 day from GSEA in WT and *Vim*$^{-/-}$ MoAMs. **b)** Heatmap of
975 normalized expression of $M_{(IL\text{-}4)}$ genes present in the leading edge of at least 1 day from
976 GSEA. Adapted Z-score normalization for each row was applied to gene expression
977 (FPKM) data. Bar graphs of gene expression (FPKM) for representative $M_{(IL\text{-}4)}$ genes
978 present in the leading edge of at least 1 day from GSEA. Error bars represent SD. **c)**
979 Heatmap of normalized expression of 186 most changed, and 254 least changed genes on
980 3dpi of the Early Inflammatory Phase. Adapted Z-score normalization for each row was
981 applied to gene expression (FPKM) data. **d)** HOMER known motif analysis using genomic
982 background of least changed genes on 3 dpi in the Early Inflammatory Phase (254 genes).
983 Motif logos are shown below motif names. Log_2(FPKM+1) average gene expression of
984 transcription factor family members are shown for WT TRAMs and WT IMs at steady-state
985 (0 dpi) and 2-6 dpi for WT MoAMs. $\log_2$FC between *Vim*$^{-/-}$ and WT MoAM gene expression
986 of transcription factor family members on each dpi. (n=3-4). **e)** Motif logos are shown
987 below motif names. -$\log_{10}$pvalues of enrichment in most or least changed gene set is
988 shown.
989
990 **Figure 7. Vimentin-deficiency in the MoAM compartment is sufficient to protect from**
991 **influenza A virus-induced lung damage and mortality. a)** Schematic of the experimental
992 design. Recipient mice (CD45.1) were irradiated and reconstituted with bone marrow cells
993 from either WT or *Vim*$^{-/-}$ donor mice (CD45.2). After a 30-day recovery period, chimeric
994 mice were intratracheally (i.t.) infected with a lethal dose of IAV at 5 days p.i. and subjected
995 to analyses. **b)** Bronchoalveolar lavage fluid (BALF) protein levels measured by Bradford
996 assay, n=3-4 **c)** Lung wet-to-dry ratio measured at day 5 p.i. n=7-10. **d**) Viral titer assessed
997 by plaque assay. n=11-14. **e)** Levels of inflammatory cytokines in BALF assessed using a
998 custom multiplex ELISA. n=4-9. Bar graphs represent mean, error bars represent SD.
999 Differences between genotypes were assessed by t-test. * $p<0.05$, ** $p<0.001$, ***
1000 $p<0.0001$, **** $p<0.00001$.
1001
1002 **Supplemental Figure 7.** Representative flow cytometry dot plots demonstrate successful
1003 engraftment of WT and *Vim*$^{-/-}$ CD45.2 donor cells into CD45.1 recipient mice.
1004